Journal of Sound and Vibration 565 (2023) 117888

Contents lists available at ScienceDirect

Journal of Sound and Vibration

journal homepage: www.elsevier.com/locate/jsvi

Large Eddy Simulation of the ACAT1 fan stage for broadband noise prediction

Danny Lewis [a,*], Stéphane Moreau [a], Marc C. Jacob [a], Marlène Sanjosé [b]

[a] Université de Lyon, Ecole Centrale de Lyon, CNRS, Institut National des Sciences Appliquées de Lyon, Université Claude Bernard Lyon I, Laboratoire de Mécanique des Fluides et d'Acoustique, UMR 5509, F-69134, Ecully, France
[b] École de Technologie Supérieure, Université du Québec, Montréal, QC H3C1K3, Canada

ARTICLE INFO

Keywords:
Aeroacoustics
Turbomachinery
Rotor–stator interaction
Broadband noise
Fan noise
Large eddy simulation
Acoustic analogy

ABSTRACT

A numerical study is carried out to assess the aerodynamic and noise radiation specific features of the ACAT1 fan stage, which was tested in the framework of the European project TurbonoiseBB. This study deals with the prediction of the broadband noise radiated by the fan stage at approach conditions, and particularly focuses on the rotor–stator interaction (RSI) noise, which results from the impact of the fan wakes onto the outlet guide vanes (OGV). To this end, two wall-modeled Large Eddy Simulations (LES) with different levels of mesh refinement have been performed on the full fan-OGV stage. The finer mesh significantly improved the aerodynamic predictions in terms of mean flow profiles, but also in terms of RMS profiles and velocity spectra, for which significant disparities are highlighted for the coarser LES. Only slight disparities regarding the turbulent content of the flow remain for the finer LES. The typical flow features at approach conditions are examined and the noise sources on both the stator and the rotor are analyzed, revealing the presence of additional broadband noise sources. Noise predictions are performed by using the free-field Ffowcs Williams and Hawkings (FW-H) analogy, and Goldstein's in-duct acoustic analogy informed with the pressure fluctuations recorded on the stator and rotor surfaces. FW-H predictions of the stator noise, though well recovering the shape of the experimental spectra, overestimate the radiated noise especially upstream of the fan. Using the finer simulation data substantially reduces the gap with the measurements. Accounting for the duct effect on the sound propagation, further improves the predictions in terms of absolute levels, leading to a good agreement between the finer simulation and the noise measurements. The breakdown of the different stator noise source contributions, in conjunction with rotor broadband noise predictions made it possible to confirm the presence of additional significant broadband noise sources, questioning the common assumption considering the RSI sources as the only dominant fan noise mechanism at approach conditions.

1. Introduction

As the regulation of noise pollution evolves towards more restrictive standards, aircraft engine manufacturers are studying innovative solutions to reduce the noise radiated by turbofan engines. On modern high bypass-ratio (HBR) turbofan engines, the fan-Outlet Guide Vane (OGV) stage has emerged as one of the major contributors to the total engine noise. Impressive reductions of

* Corresponding author.
E-mail addresses: danny.lewis@onera.fr (D. Lewis), stephane.moreau@usherbrooke.ca (S. Moreau), marc.jacob@ec-lyon.fr (M.C. Jacob), marlene.sanjose@etsmtl.ca (M. Sanjosé).

https://doi.org/10.1016/j.jsv.2023.117888
Received 18 October 2022; Received in revised form 29 May 2023; Accepted 18 June 2023
Available online 21 June 2023

the engine noise have been achieved by a continuing increase of the bypass ratio since the early 70's. A variety of techniques have been deployed or are still on the test bench to gain additional decibels. Among these, the use of surface treatments on the nacelle, such as acoustic liners, smart blade/vane counts exploiting the duct cut-off properties, revisited blade and vane geometries, have already led to a significant reduction of the tonal component of the fan stage noise. Nevertheless, little progress has been made to reduce the broadband noise so far. Reducing fan broadband noise has indeed appeared as more challenging since it results from complex flow mechanisms involving the interaction of turbulent structures with solid surfaces such as the ingestion of atmospheric turbulence, the turbulent boundary layers developing on the duct walls and on the fan and OGV surfaces, the rotor tip-clearance flow, or the impingement of the fan turbulent wakes onto the OGV row [1,2]. The latter, which is also referred to as the Rotor–Stator Interaction (RSI), has been identified as one of the dominant broadband noise sources on current engines. Its contribution is expected to increase in future Ultra High Bypass Ratio (UHBR) engines, that will have larger fan diameters along with a shorter rotor–stator spacing. In order to develop tailored noise mitigation solutions, the broadband noise sources have to be accurately assessed. To this purpose, it is paramount to develop the capability of understanding the underlying flow mechanisms more precisely. An extensive range of approaches has been developed to predict the broadband noise generated by the aforementioned mechanisms, especially the RSI, with a variety of approaches ranging from semi-analytical to fully numerical modeling. More precisely, semi-analytical approaches such as RANS-informed analytical models, are based on linearized modeling of the unsteady aerodynamics past slender airfoils. They are best suited for pre-design studies, given their relatively low cost and their reasonable accuracy. Conversely, high order methods such as Direct Numerical Simulations (DNS) of the fully compressible time-dependent Navier–Stokes equations, may provide highly accurate noise estimates but require prohibitive computational resources and are thus not eligible for the complex high Reynolds number configurations encountered in turbomachinery applications (see Lewis et al. [3] Moreau [2], Moreau & Roger [4] and Wang et al. [5] for a comprehensive review of the available approaches).

In the context of fan-OGV stage noise, the hybrid numerical approaches are the focus of a growing interest as they provide accurate noise assessments at a much more affordable cost than DNS. They couple a fully unsteady scale resolving simulation with an acoustic analogy, such as Ffowcs Williams and Hawkings' (FW-H) analogy [6], the Kirchhoff analogy, or the Goldstein duct analogy [7], to recover the acoustic far-field. Hybrid numerical approaches are subdivided into two different branches. On the one hand, the scale resolving computations are used to compute both the noise sources and the resulting acoustic near-field. The porous formulation of Ffowcs Williams and Hawkings' analogy is then used to compute the acoustic far-field based on the acoustic near-field recorded on porous surfaces located at the edge of the computational domain. Such an approach was successfully applied to fan-OGV stages by Gonzalez-Martino and Casalino [8] and Casalino et al. [9,10] using the Lattice Boltzmann Method (LBM), and by Leonard et al. [11] using a wall-modeled LES. On the other hand, the simulation only computes the noise sources in order to reduce the computational cost. The unsteady loading on the rotor blade and stator vane surfaces is directly retrieved from the simulation and used as a dipole source distribution in the framework of a chosen acoustic analogy. This approach has been extensively used to compute the noise produced by fan-OGV stages [11–17] because it is much less CPU-demanding than the first one since the computation of the acoustic near-field is not required. The main drawback of this approach is that the sound propagation is exclusively performed through an acoustic analogy, the accuracy of which is directly dependent on the chosen Green's function. The Green's functions are indeed known only for canonical cases (free-field, uniform flow, annular and cylindrical ducts, with possible but complex extensions to slowly varying ducts, lined ducts, mean swirling flows), which prevents from fully taking into account the complexity of the geometry inside of the nacelle for instance (rotor shielding effect, sudden change of the duct cross-section at the bypass/core flow splitter location).

The aim of this article is to assess the capacity of the hybrid approach using the unsteady loading on the rotor and stator surfaces to provide reliable fan stage noise predictions with a Wall-Modeled LES (WMLES) as the chosen scale-resolving simulation approach. It is an extension of a previous work presented by Lewis et al. [17] who performed a medium sized WMLES on the ACAT1 configuration tested in 2018 in the ANECOM UFFA facility in Wildau (Germany) in the framework of the European project TurbonoiseBB [18–21]. In the latter study, the RANS and LES-informed analytical predictions and the hybrid numerical predictions revealed the presence of additional non-RSI dominant noise sources, the magnitude of which was comparable to that of the RSI sources. However, the level of grid refinement, though meeting the mesh requirements for WMLES, showed its limits and the need for a finer simulation. A refined WMLES (named LES2 hereinafter) is presented in the following study and directly compared to the WMLES already presented by Lewis et al. [17] (named LES1 hereinafter) and to Lewis et al.'s RANS study using a wall-resolved $k-\omega$ SST RANS simulation [22]. A comprehensive analysis of the flow topology and of the noise sources at approach flight conditions is carried out, as well as broadband noise predictions using both FW-H's and Goldstein's analogies. François et al. [23] and Polacsek et al. [24] also carried out a comprehensive study on the ACAT1 fan stage at approach condition, with consistent results with the present study, using a different scale resolving simulation approach, namely the ZDES [25].

In Sections 2 and 3, the experimental and numerical set-ups are presented respectively. Aerodynamic results are discussed in Section 4, whereas Section 5 is devoted to acoustic results.

2. Turbofan configuration

The ACAT1 turbofan model consists of 20 fan blades and 44 stator vanes. Two configurations have been tested: one with a short fan-OGV gap and an additional one with a longer rotor–stator gap. Fig. 1 displays these two configurations along with the measuring instruments for both the acoustic and the aerodynamic measurements. Ring arrays were used for the acoustic measurements at the inlet (CMD1), interstage (ISTG) and bypass (CMD3) sections, and axial arrays at the interstage and in the bypass duct (AX1). The Wave Number Decomposition (WND) technique [26–28] was applied to the latter in order to compute the downstream noise

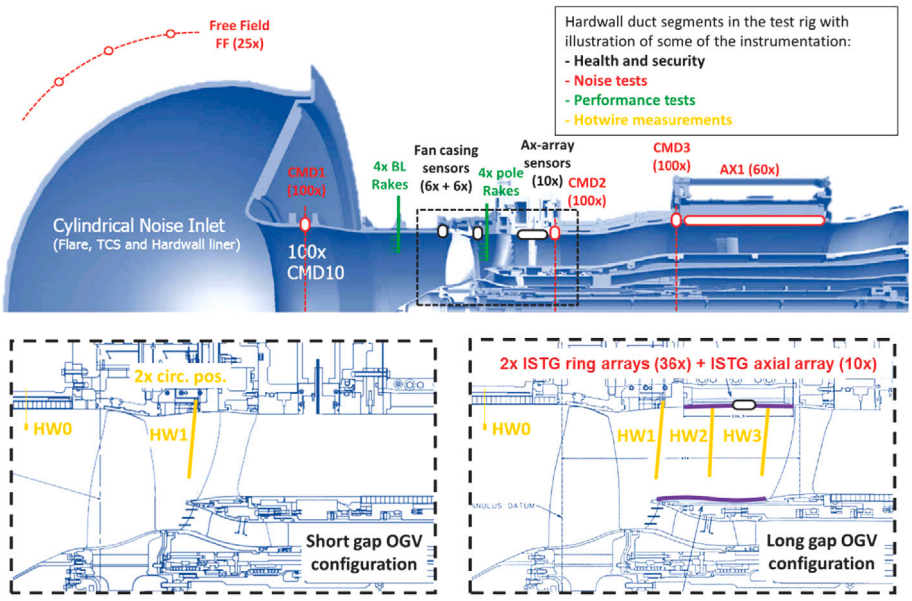

Fig. 1. View of the UFFA fan rig of AneCom AeroTest.

Table 1
Approach condition.

Geometrical parameters	Tip radius (m)	0.435
	Hub radius at the rotor leading edge (m)	0.138
	Rotor mid span chord $c_{\text{midspan,R}}$ (m)	0.136
	Stator mid span chord $c_{\text{midspan, S}}$ (m)	0.066
	Rotor tip gap (mm)	0.78
	Rotor–stator spacing	$\approx 1.3 * c_{midspan,R}$
Operating point	Rotational speed (rpm)	3828.2
	Tip relative Mach number	0.57
	Total mass-flow rate (kg/s)	55.156
	Bypass ratio	7.6
	Ambient pressure (hPa)	995.6
	Ambient temperature (K)	292.8

spectrum [20] that serves as a reference for the acoustic predictions. Moreover, an array of 25 microphones, equally distributed from 0 to 120 degrees along an arc of radius 18.5 m centered on the fan axis at the nozzle inlet, was used for far-field sound measurements upstream of the inlet. The resulting noise spectrum is used in the following study as a reference for upstream noise validations. Hot-wire measurements were performed upstream of the fan (HW0 position) and in the interstage at several axial locations (HW1, HW2, HW3) for the long-gap configuration, whereas for the short-gap configuration, only the position HW1 was explored in the interstage. Both configurations were tested at different operating conditions (approach, sideline and cutback conditions) on two different working lines (SLS and LN) that differ by the blade loading of the fan. The present paper focuses exclusively on the SLS working line, at approach condition, for the short-gap configuration. The hot geometry of the fan blades, which accounts for the deformation of the fan blade induced by the rotational speed, is used in the present study. The flow conditions of this operating point as well as some details about the stage geometry are given in Table 1.

3. Numerical setups

3.1. Computational domain

LES2 computational domain is strictly identical to that of the LES1 presented by Lewis et al. [16]. The use of periodic boundary conditions, along with the reduction of the OGV-vane count from 44 to 40 (9% reduction), made it possible to restrict the simulation domain to an 18 degree passage consisting of one fan blade and two OGV vanes. In order to maintain the stage performance, a rescaling of the OGV vane was performed by ONERA [29] following Rai and Madavan's [30] method, which consists of an axial and a azimuthal rescaling (increase by a factor 9%) that preserves the solidity, the thickness to chord ratio and the camber line of the original OGV row, while maintaining parameters such as the rotor–stator spacing and the sweep, lean and stagger angles, which

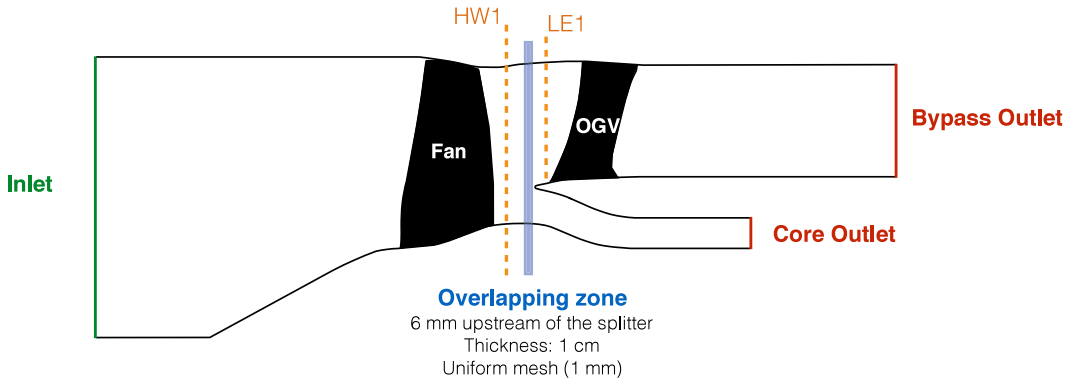

Fig. 2. Computational domain. HW1 and LE1 correspond to the location of the axial cuts performed in the LES simulations. Hot-wire measurements have been performed at the HW1 position.

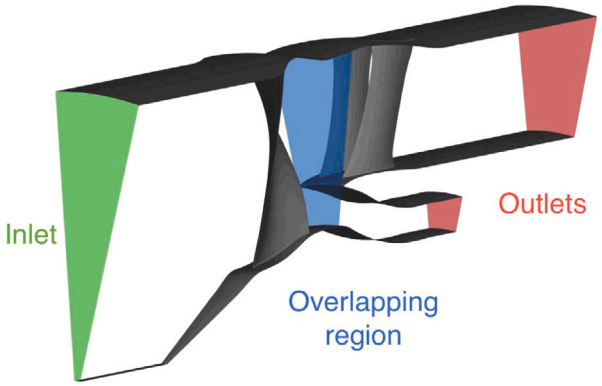

Fig. 3. LES computational domain.

are determinant for broadband noise predictions. The vane count modification is expected to have a significant impact on the tonal component of the noise, especially regarding its magnitude at the Blade Passing Frequency (BPF) and its harmonics. Only a limited effect on the broadband noise is expected as shown by Leonard et al. [11] who performed a similar geometric transformation on the Source Diagnostic Test (SDT) configuration. A RANS study showing that the rescaling has had almost no impact on the performance parameters, on the pressure distribution on the OGV skin, and on the RSI broadband noise is presented in Appendix B of Lewis [31]. The meridional view and the 3D view of the final computational domain is depicted in Figs. 2 and 3.

The Inlet Guide Vanes (IGV) of the primary flow have been removed from the computational domain, since the broadband noise resulting from its interaction with the fan is considered as relatively negligible at this operating point.

The computational domain extends from 4 fan axial chords upstream of the rotor at mid-span, to 6 vane axial chords downstream of the stator also at mid-span. Two main reasons have led to the choice of these dimensions:

- They allow the boundary layers to develop on both the spinner and the casing upstream of the rotor.
- The core and bypass exhaust boundary conditions are easier to control especially regarding the reflection of sound waves.

3.2. Numerical parameters

3.2.1. Solver

The AVBP code developed by Cerfacs [32], has been used to carry out the compressible LES on the ACAT1 configuration for its capability to accurately address turbomachinery configurations. The method used consists of the coupling of two LES domains, the first one dedicated to the rotor, and the second one to the stator. The two computational domains are coupled using an overset grid method [33], implemented using the coupling library CWIPI, through which conservative variables are exchanged between the two instances. The filtered compressible Navier–Stokes equations describing the mass, momentum and energy equations for a perfect gas are solved. Equations are solved using a finite-volume Lax–Wendroff time explicit scheme with second-order accuracy in time and space [34]. The CFL number has been set to 0.7 to ensure the stability of the numerical simulation. The Wall-Adapting Local Eddy-viscosity (WALE) subgrid-scale closure, developed by Nicoud and Ducros [35], is used to model the unresolved turbulent contributions.

Table 2
Numerical parameters.

	Time step (s)	Number of iterations per blade passages
LES1	$3.7 \cdot 10^{-8}$	22 000
LES2	$2.75 \cdot 10^{-8}$	29 000

Table 3
Number of points to discretize the fan blade surface.

	Streamwise direction	Spanwise direction
LES1	150	200
LES2	250	300

Table 4
Number of points to discretize the OGV blade surface.

	Streamwise direction	Spanwise direction
LES1	100	150
LES2	150	250

Table 5
Wall mesh requirements for LES [45,46].

	Wall-resolved LES	Wall-modeled LES
s^+	50–150	100–600
r^+	10–40	100–300
n^+	1	30–150
Number of points in $0 < n^+ < 10$	3–5	–

3.2.2. Boundary conditions

The inlet and outlets are treated using non-reflecting Navier–Stokes Characteristic Boundary Conditions (NSCBC) [36]. At the inlet, the experimentally measured total temperature and pressure are imposed and the flow is purely axial with no turbulence injection [37]. At the outlet, the flow reaches a radial equilibrium that matches the mean static pressure extracted from a surface average of the static pressure at the outlet of the RANS simulation. Periodic boundaries are imposed on both lateral sides of the domain. On all the solid walls, the boundary layer is modeled using a wall law inducing a no-slip condition at the walls (see the work of Nicoud et al. [38] for more details on the law itself). A linear law is imposed if the normalized wall distance is $y^+ < 11$, and a logarithmic law otherwise (Schmitt et al. [39]).

The time step as well as the number of iterations per blade passage for both simulations are displayed in Table 2.

The present numerical method has been validated on compressors [40], turbines [41] and turbofans [11–13,16,17,42] and has recently led to first fully coupled engine simulations [43,44].

3.3. Unstructured mesh

The Centaur software was used to generate the LES grid, which is made of prism cells on the walls and of tetrahedra cells elsewhere. The LES2 mesh topology is globally the same as that of LES1 [16]. Finer mesh parameters than for LES1 have been used to improve the accuracy of the simulation both near the walls and in the volume. The surface mesh has been significantly refined by increasing the number of points to discretize the rotor blade and stator vane surfaces with respect to the LES1 mesh, with a finer description of the leading edge and trailing edge curvature and an increased surface cell density over the entire vane and blade span. LES2 surface mesh is almost 1.5 finer than that of LES1 as shown in Tables 3 and 4, which summarize the refinement differences in the axial and radial directions for the fan blade and the OGV vane surfaces, respectively. The number of prism layers in the near wall region has been increased from 8 in LES1, to 14 in LES2 to better capture the boundary layer and possible flow separation.

In the case of wall-modeled LES, the dimensionless wall distance to a surface in the normal direction (designated either by y^+ or n^+), and in the tangential directions (s^+ for the streamwise direction and r^+ for the third local direction) have to cope with certain requirements [45,46] that are recalled in Table 5 along with the wall-resolved LES requirements.

The n^+ values in the entire computational domain are shown for LES2 in Fig. 4. Figs. 5 and 6 show a closer look at the n^+, s^+ and r^+ values on the blade and vane skins, confirming that the mesh is consistent with the wall requirements for wall-modeled LES. Table 6 summarizes the improvement of the wall mesh from LES1 to LES2.

The volume mesh has also been significantly refined from LES1 to LES2 in key zones such as the blade and vane leading edge (LE) and trailing edges (TE), as well as the interblade and intervane regions, the rotor tip clearance and the wakes. These zones are highlighted in Figs. 7–10, which give an overview of the topology of the mesh.

The resulting number of mesh cells for each simulation is detailed in Table 7.

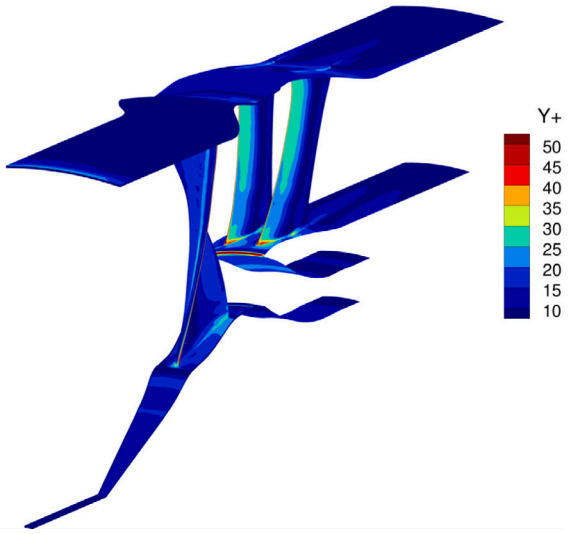

Fig. 4. n^+ values.

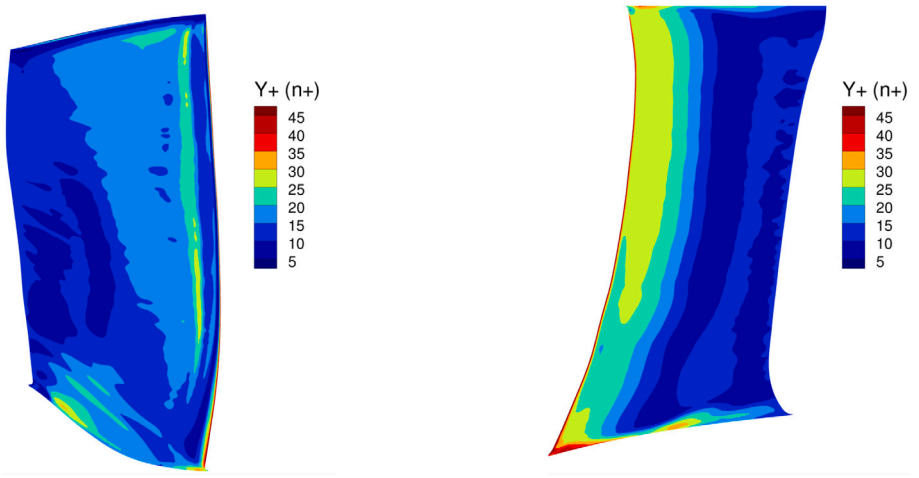

(a) Rotor. (b) Stator.

Fig. 5. n^+ values on the rotor and stator suction sides.

Table 6
n^+, s^+ and r^+ maximum and average values on rotor blade and stator vane surfaces.

	Mean n^+	Maximum n^+	Mean s, r^+	Maximum s, r^+
LES1	25	66	80	300
LES2	17	64	64	195

Table 7
Mesh size: number of cells per subdomain.

	Rotor ($\cdot 10^6$)	Stator ($\cdot 10^6$)	Total ($\cdot 10^6$)
LES1	56	39	95
LES2	125	85	210

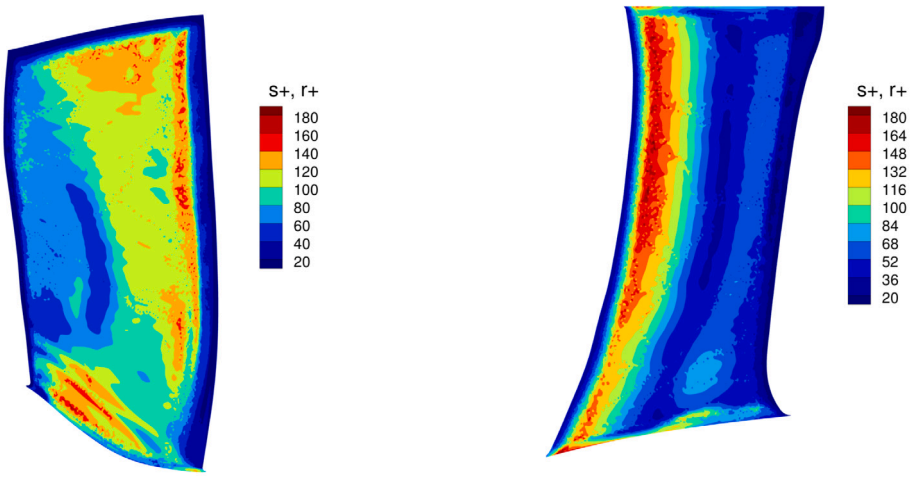

(a) Rotor. (b) Stator

Fig. 6. s^+ and r^+ values, rotor and stator suction sides.

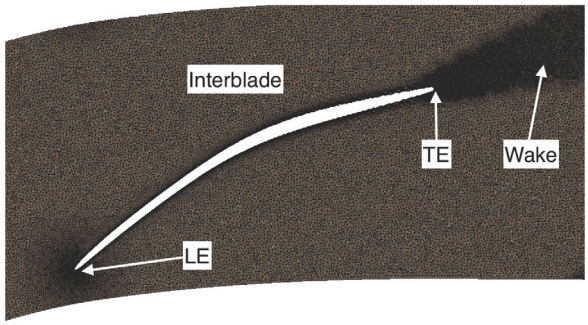

Fig. 7. Midspan radial cut of the rotor domain mesh.

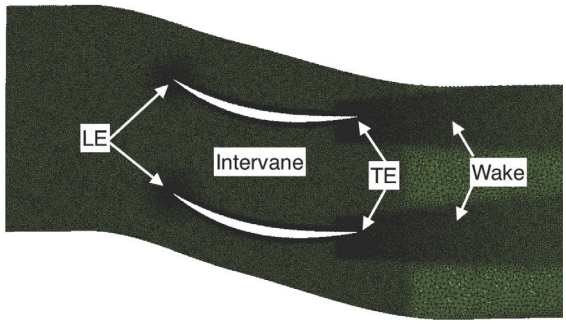

Fig. 8. Midspan radial cut of the stator domain mesh.

3.4. Convergence and extractions

The convergence monitoring strategy is similar to that used by Lewis et al. [17] for the LES1 simulation. The convergence of the mean flow has been checked by monitoring common integrated quantities (mass-flow rate at the inlet and outlets, fan pressure ratios in the bypass and core flows) as well as local quantities such as the pressure or the velocity using local control points (hereafter referred to as "probes"), the locations of which are shown in Fig. 11. The probes located upstream of the splitter are fixed in the rotating frame of reference. The stabilization of integrated quantities ensures the convergence of the mean flow. The convergence of flow statistics has been checked by analyzing the signals retrieved from the probes with the method developed by Mockett

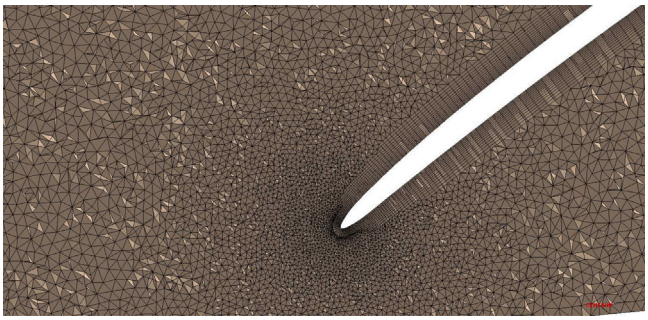

Fig. 9. Rotor blade leading edge mesh.

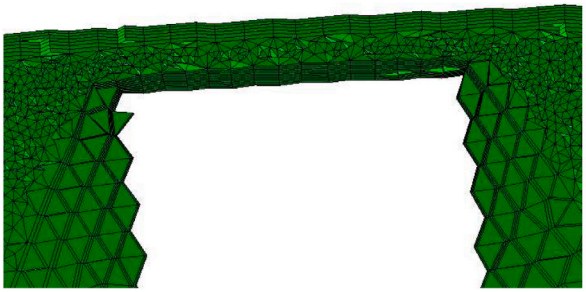

Fig. 10. Rotor blade tip gap mesh.

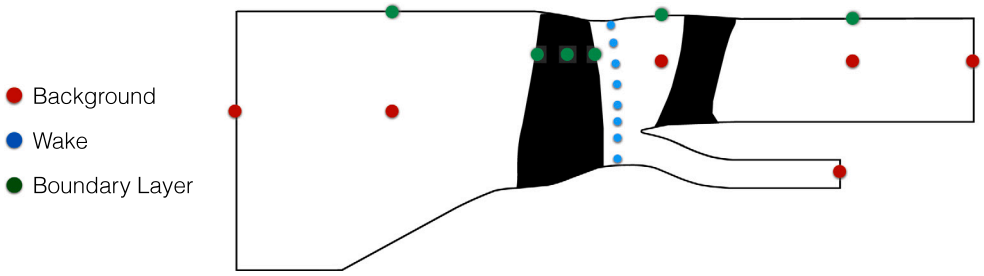

Fig. 11. Locations of probes.

et al. [47]. This method enables to estimate the statistical error of a finite time signal and is particularly suited to identify the end of the transient regime of an LES. It has been applied to all the probes to start data acquisition for statistics as early as possible.

Since the LES2 was initialized from an instantaneous solution of the LES1, the transient regime was shortened down to 1.7 fan rotations. The statistics were recorded for about three rotations over which the wall-pressure fluctuations on the rotor blades and the stator vanes were extracted, as well as the pressure and velocity components at the three axial positions shown in Fig. 2 (IN1, HW1 and LE1). These flow extractions were performed every 300 time-steps, which corresponds to a sampling rate of about 120 kHz. The details related to the Fourier transform of each simulation signal are summarized in Table 8 and are valid for all the signal post-processing of this article.

4. Aerodynamic analysis

4.1. Performance parameters

Tables 9 and 10 present the performance parameters at approach condition obtained from the RANS computation and from the two LES. These values have been obtained from a mass-flow rate weighted average over an axial field cut at the splitter location, upstream of the stator. The agreement of the RANS results with the experimental data is excellent within the measurement

Table 8
Fourier transform parameters for the PSD computations.

	LES1	LES2
Sampling frequency (kHz)	110	120
Number of averaging windows (Hann windows)	10	5
Overlap	50%	50%
Δf (Hz)	282	206

Table 9
Mass-flow rates obtained from the simulations at approach condition.

	Massflow rate (kg/s)		
	Bypass	Core	Total
Experiment	48.745	6.411	55.156
RANS	48.745	6.411	55.156
LES1	48.787 (+0.09%)	6.395 (−0.25%)	55.186 (+0.05%)
LES2	50.108 (+2.8%)	6.500 (+1.4%)	56.647(+2.7%)

Table 10
Fan pressure ratios obtained from the simulations at approach condition.

	Fan pressure ratio		
	Bypass	Core	Total
Experiment	1.110	1.100	1.109
RANS	1.106 (−0.36%)	1.098 (−0.2%)	1.105 (−0.34%)
LES1	1.106 (−0.36%)	1.095 (−0.45%)	1.105 (−0.36%)
LES2	1.109 (−0.01%)	1.098 (−0.19%)	1.107 (−0.18%)

uncertainty: the computed bypass pressure ratio is close to the experimental value (0.36% error) as well as the pressure ratio of the core flow (0.2% error). The total Fan Pressure Ratio (FPR), computed from the mass-flow rate weighted average of the core and bypass FPR, is also close to the experimental data. Similar comments can be made for the performance parameters obtained with LES1. Regarding LES2, however, larger discrepancies are observed, especially in the bypass flow. This is mainly due to a significant modification of the flow topology on the stator vane, which will be shown in the following sections. François et al. [23] also showed that using a total pressure profile at the inlet of the domain, along with an adjustment of the downstream static pressure resulted in a massflow rate closer to the one measured in the experiment. Adjusting the outlet pressure in the present case might have resulted in larger discrepancies regarding the pressure ratios, which would not have improved the results either. The same outlet pressure was thus prescribed for both LES. The fact that François et al. [23] used reflective boundary conditions along with sponge zones also made it possible to impose more strictly the boundary conditions than with NSCBC, the latter allowing for a slight drift of the values prescribed at the boundary while being more efficient for handling acoustic wave reflections.

4.2. Mean flow topology

4.2.1. Main flow features

The streamlines of the mean flow colored by the mean vorticity magnitude shown for the three computations in Figs. 12 and 13 give a first overview of the mean flow topology on the rotor and stator suction sides, respectively. The rotor streamlines are shown in the relative frame of reference.

In the case of the rotor, all simulations exhibit a strong radial flow with streamlines leaving the rotor TE at a much higher radial position than at the LE. This is particularly noticeable in both LES for which streamlines that are close to the hub at the LE, leave the fan at the TE at almost 70% rotor span. In all simulations, a strong radial vortical structure develops at the LE of the fan. In the RANS, it extends from 40% rotor span up to the tip and displays a sawtooth profile. Its radial extent is much longer in both LES, covering almost 80% of the rotor span. In both LES, this radial structure appears to be partly formed of streamlines that originate from the lower part of the fan LE and travel up to the rotor tip, where they eventually feed the tip gap flow. This phenomenon is less visible in the RANS case as most of the streamlines originally caught in this structure leave it to continue their path down to the trailing edge. In the RANS, the streamlines originates from the upper part of the fan LE, while the lower part streamlines directly feed the tip gap flow in both LES. Such a radial structure was also observed in Kissner et al.'s RANS study on the ACAT1 fan stage at approach condition (see Fig. 5 in [48]) and by Pérez Arroyo et al. [49] and Kholodov et al. [15,50] on the SDT configuration at approach condition, suggesting that it is a characteristic flow feature at low fan speeds. Furthermore, in all simulations, LE streamlines that are not necessarily caught in the radial vortex appear to move alternatively towards the upstream and downstream directions, indicating a potential flow recirculation.

Regarding the flow around the stator, the RANS displays streamlines that are aligned with the stage axis over most of the OGV span. A slight radial flow can be observed near the hub and the shroud where the boundary layers on the duct walls interact with the flow near the vane surface. Both LES display significant differences with the RANS simulation. From the leading edge down

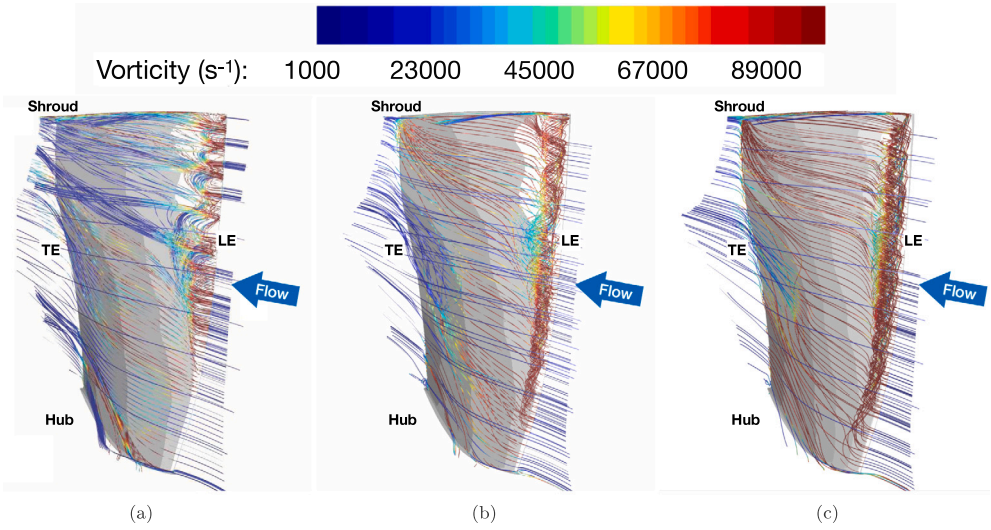

Fig. 12. Streamlines in the rotor domain (suction side). (a) RANS, (b) LES1, (c) LES2. (For interpretation of the references to color in this figure legend, the reader is referred to the web version of this article.)

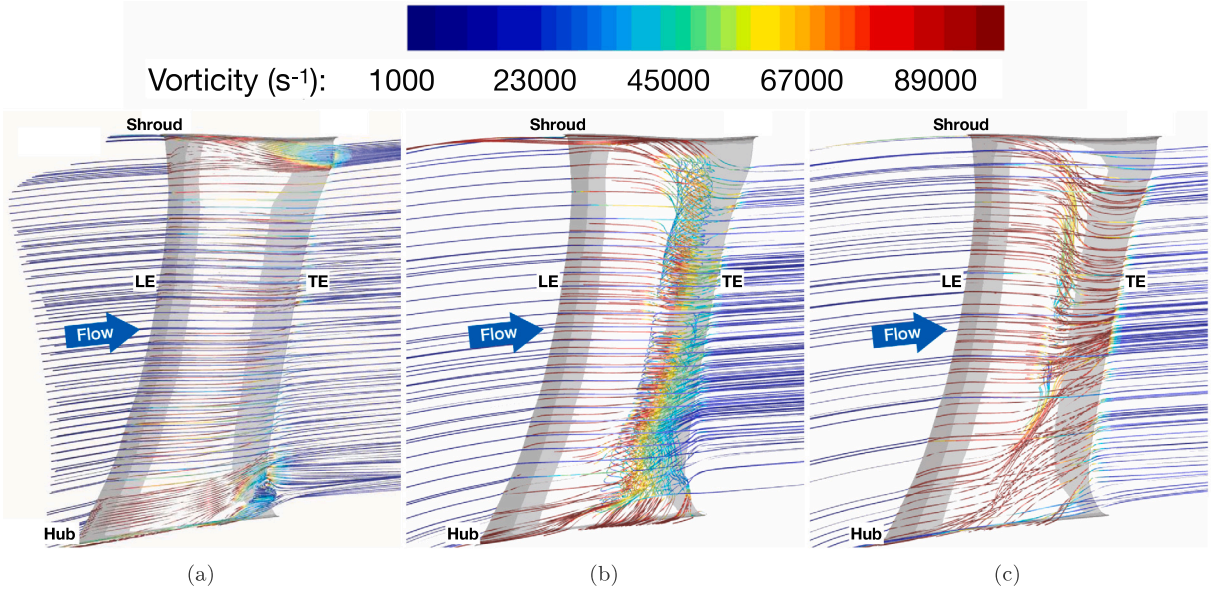

Fig. 13. Streamlines in the stator domain (suction side). (a) RANS, (b) LES1, (c) LES2. (For interpretation of the references to color in this figure legend, the reader is referred to the web version of this article.)

to 60% stator chord, the flow remains aligned with the axial direction, as observed in the RANS results. From that point, a radial flow, which tends to bring the streamlines closer to the stator midspan can be observed in both LES. LES1 displays an intense radial vortical structure at 60% stator chord extending over the entire vane span. This vortical structure is very similar to the one observed at the rotor LE and is mainly composed of streamlines originating from the duct wall boundary layers. As with the rotor, its structure reveals that a recirculation occurs in this region. The radial vortex is however not present in LES2, which suggests that it is a consequence of a lack of mesh refinement in LES1.

The identified recirculation regions strongly contribute to the creation of turbulent structures near the blade and vane surfaces as shown by the Q-criterion isosurfaces displayed in Figs. 14 and 15 for both LES.

The first view presented in Fig. 14 shows the development of the turbulent structures on the rotor suction side that result from the LE flow separation. Larger coherent structures are created in LES1, whereas LES2 displays an increased concentration of smaller structures. This contrast is partly related to the presence/difference of the LE flow detachment intensity, such as below 20% of the rotor span where the flow is clearly turbulent in the case of LES2, but quasi-laminar in LES1. They also illustrate the more accurate

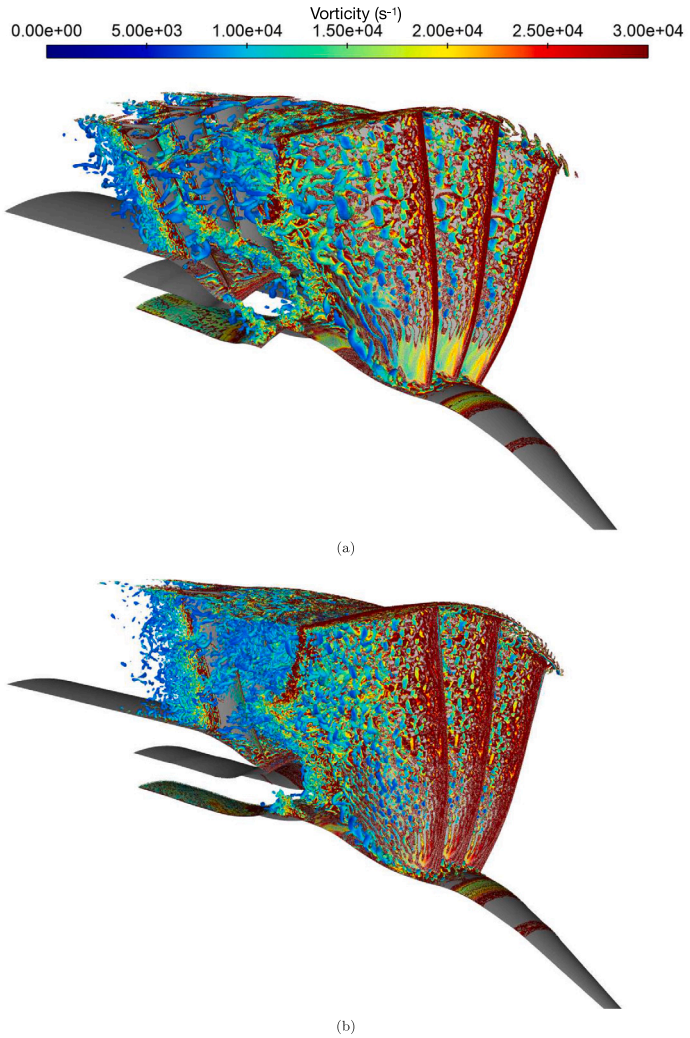

Fig. 14. Q-criterion iso-surface colored by the vorticity magnitude (front part view). (a) LES1, (b) LES2. (For interpretation of the references to color in this figure legend, the reader is referred to the web version of this article.)

description of turbulence resulting from the finer mesh of LES2. The aforementioned radial flow is also well illustrated in these pictures.

The different patterns of the turbulent structures along the blades have a direct influence on the structure of the downstream wakes, which are mainly made of large stretched structures in LES1, while both elongated and smaller structures can be observed in LES2. A horseshoe vortex forms at the junction of the rotor leading edge and the hub in both simulations. Its vortical structure is well captured by LES2 while it appears to be smoother in LES1. On the stator pressure side, the flow seems to remain laminar over the whole vane axial extent.

Fig. 15 shows a view of the rear part of the computation domain. It confirms the previous observations made on the rotor wakes. For the chosen iso-surface value, the LES1 wakes look scattered compared to the dense LES2 wakes, which are well defined throughout the inter-vane channel. For both simulations, the flow is laminar on the whole rotor blade pressure side, except on isolated turbulent spots and between 10% and 60% of the rotor span near the trailing edge. The second leg of the horseshoe vortex can be observed. Once again, its vortical structure is much clearer in LES2 than in LES1. Regarding the flow on the vane, the boundary layer is quasi-laminar from the LE down to 65% of the vane chord. It then transitions to turbulence in both computations. This transition is more abrupt in LES1 because of the significant flow separation occurring at this location.

4.2.2. Friction line analysis

As highlighted in the above section, flow separations can be observed on both the fan and the OGV. They are actually quite common at approach condition since the fan is operating in off-design conditions, that is, at higher angles of attack than in cruise

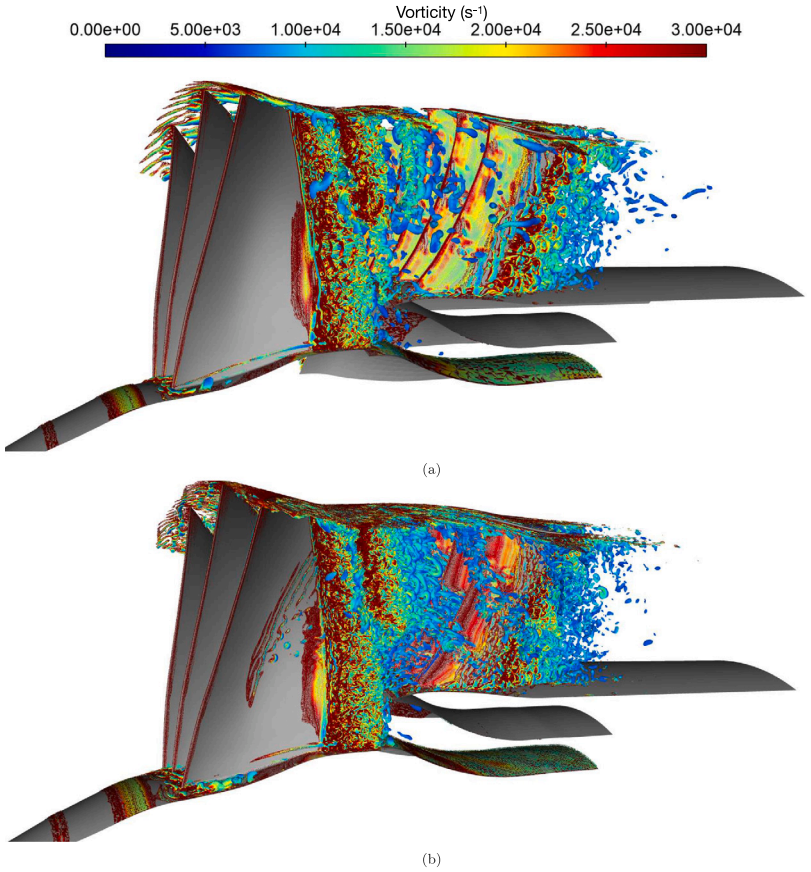

Fig. 15. Q-criterion iso-surface colored by the vorticity magnitude (rear part view). (a) LES1, (b) LES2. (For interpretation of the references to color in this figure legend, the reader is referred to the web version of this article.)

condition. In order to have a better view of the zones affected by such flow separations, the mean friction coefficient C_f has been computed on the suction side of the blades and vanes and is plotted in Figs. 16 and 17 along with the streaklines. C_f is defined as follows:

$$C_f = \frac{\tau_w}{\frac{1}{2}\rho_\infty V_\infty^2}, \tag{1}$$

where ρ_∞ and V_∞ are the density and the velocity of the fluid at the inlet, respectively. τ_w is the wall shear stress defined as:

$$\tau_w = \mu \left(\frac{\partial V_s}{\partial n} \right)_{wall}, \tag{2}$$

where μ is the dynamic viscosity of the fluid, V_s is the flow velocity tangent to the wall and $\left(\frac{\partial V_s}{\partial n}\right)_{wall}$ is the wall value of the derivative of V_s in the wall normal direction.

Fig. 16 reveals that the previously observed flow separation at the fan leading edge actually covers 75% to 95% of the rotor span and the first 15% of the rotor chord, which includes the area covered by the LE radial vortex. In the case of the RANS, the flow separation extends from 25% of the fan span up to the tip of the rotor. In both LES, it covers a longer area and seems to be divided into two parts over most of the blade span, as suggested by the friction lines. However, this splitting of the detached area seems to result more from the averaging process than from a real behavior of the flow. Indeed, as it will be shown in the analysis of the unsteady flow (Section 4.4), the intermittent behavior of the separation bubble results in fluctuations of its size that may lead to such a mean solution, as also observed by Deuse and Sandberg [51] and Wu et al. [52] in their study of a Controlled Diffusion (CD) airfoil geometry similar to one used on both the SDT and ACAT1 blades. Such a flow separation was also observed on the ACAT1 fan stage at approach condition using other simulation approaches such as Zonal Detached Eddy Simulation (ZDES) (see [14,29]), Zonal Large Eddy Simulation (ZLES) (see Fig. 11 in Tucker and Wang's review paper [53]), and RANS (see [48]). Al Am et al. [54] also observed a similar structure using a wall-resolved LES approach on a fan-OGV configuration of limited span extent.

In the RANS case, the flow reattaches downstream of this flow separation before reaching half the blade chord and remains attached down to the trailing edge. For both LES, the flow reattaches before reaching a quarter of the blade chord and remains

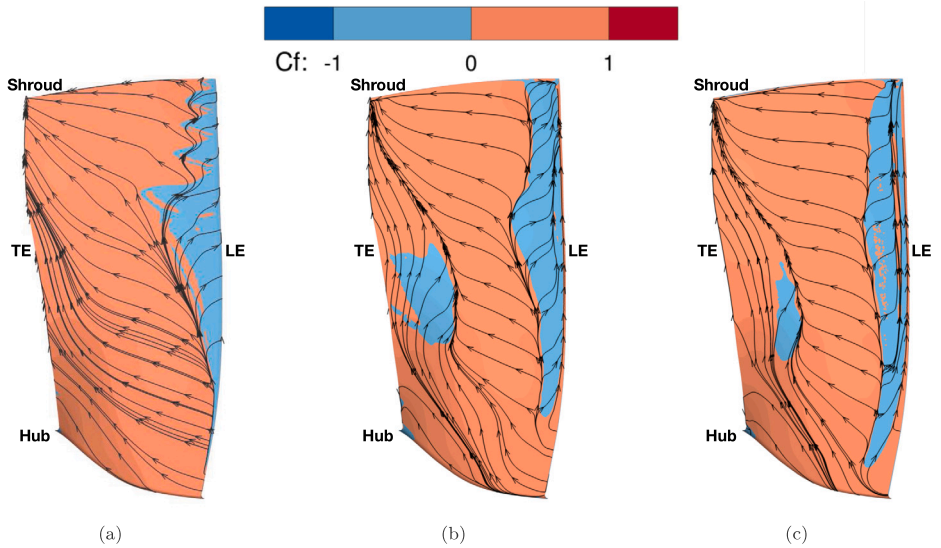

Fig. 16. Mean friction coefficient and streaklines on the fan suction side. (a) RANS, (b) LES1, (c) LES2.

attached down to the trailing edge except between 30% and 60% of the rotor span, where a second flow detachment occurs at 60% rotor chord. In LES2, this second flow separation has a shorter streamwise extent than in LES1.

Regarding the vane (Fig. 17), significant differences can be observed between the three simulations. For the RANS, the flow remains attached on almost all the suction side. Small isolated separation zones appear at the LE close to the casing and at the TE at 10% vane height. LES1 displays a radically different flow pattern, with a substantial flow separation occurring at around 65% stator chord, which extends over almost the entire vane span and coincides with the radial vortex observed in Fig. 13. Between 20% and 95% of the vane span, the flow reattaches before reaching the trailing edge while below 20% it remains detached. This flow separation disappears in LES2 as a result of the wall mesh refinement, which has led to a better description of the near wall flow. This reveals that wall laws should be used with caution since wall-mesh requirements for WMLES are actually quite broad. Thus, two WMLES complying with these requirements may exhibit significant discrepancies, as in the present case. The study of Polacsek et al. (Figure 13 in [24]) also revealed that the simulation of the rear part of the stator can be tricky as it displays complex flow patterns and exhibits unexpected flow detachments. Furthermore, even though the present WMLES are able to predict large flow detachments, it should be noted that they might fail to accurately predict the exact detachment and reattachment points. The overall flow topology of both LES is still quite similar and differs from that predicted by the RANS that fails to capture the radial secondary flows.

4.3. Wake analysis

4.3.1. Mean wake profiles

Broadband interaction noise directly depends on the characteristics of the turbulence impinging upon the stator row. Statistics of the radiated sound field are expected to depend on statistics of the turbulence, in particular its wavenumber content, as the unsteadiness felt by the vanes is mostly due to the spatial flow inhomogeneities convected past the leading edge. The overall envelope of the radiated field is shaped by the cascade response but modulated and shifted by the average turbulence parameters, and convection velocity of the turbulent eddies. As a consequence, typical turbulence variables such as the turbulence kinetic energy (TKE) within and outside of the wakes, and the flow characteristic dimensions (wake width, integral length scale) are usually prescribed as input parameters for analytical models for broadband RSI noise predictions. They notably have a substantial effect on the subsequent noise predictions [55]. An accurate simulation of these flow characteristics is then compulsory to ensure the reliability of the noise predictions, whether numerical or analytical.

Because of a HW calibration issue during the AneCom tests, a post-test recalibration was performed on the raw data by the team in charge of the measurements to correct a detected offset [56,57], giving rise to the more accurate data used in the present study. Fig. 18 shows the average values of the three velocity components and of the TKE measured by the HW at the HW1 position retrieved from the re-calibrated data set. The axial velocity (Fig. 18(a)) and TKE (Fig. 18(d)) contours reveal significant wake-to-wake variations: some blades are shedding particularly thick wakes with intense TKE levels (wake at 4 o'clock), while others produce very thin wakes with low TKE levels (wake at 10 o'clock). Slight blade-to-blade geometrical differences in the experiment, in conjunction with the choice of an operating point far off-design, may have affected the LE rotor flow separation in terms of magnitude and chordwise extent, resulting in downstream wake disparities. This lack of axisymmetry, also observed at cutback and sideline operating points to a lesser extent, prevents from precisely appreciating the accuracy of the wake simulations. In order to

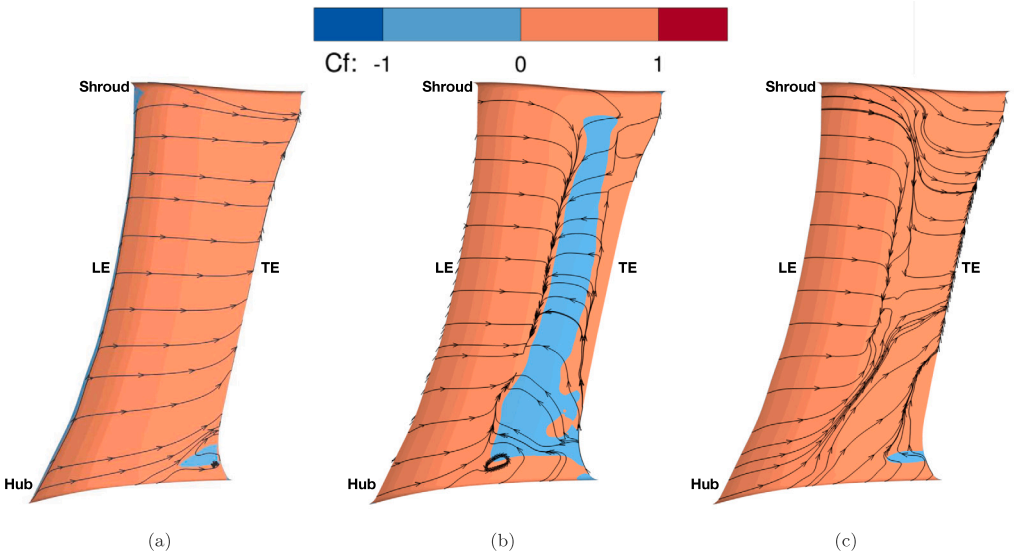

Fig. 17. Mean friction coefficient and streaklines on the vane suction side. (a) RANS, (b) LES1, (c) LES2.

have a quantitative analysis, the mean and RMS azimuthal profiles of each velocity component have been plotted for different radial positions, along with the corresponding experimental revolution range. The latter estimates the range of variations observed in the experimental data at each radius, and over the full annulus. Thereby, the blade-to-blade variations are taken into account without isolating each wake.

At 25% rotor span (Fig. 19), the experimental revolution range is remarkably thinner than at other radial positions, indicating smaller blade-to-blade variations. Regarding the axial velocity, the RANS profile are in good agreement with the experimental data. Indeed, the velocity deficit is well predicted and the velocity in the background flow matches the experimental values. Both LES underestimate the velocity deficit, but recover the background values. However, the three simulations tend to predict a wake that is thinner than in the experiment. Both azimuthal and radial velocities are overestimated by the simulations, the RANS results being the closest to the experimental data. The overall shape of the experimental profile is well recovered by all simulations, which ensures that the correct behavior of the flow is captured. The discrepancy between the experimental and numerical mean azimuthal velocity appears to be larger than it actually is, due to the scale chosen for the y-axis: it lies indeed within around 10% of the azimuthal velocity. As for the radial component, it is only about 1/10th of the other components: therefore a small error on the axial or azimuthal component results in a strong error on the radial velocity. In LES1, however, an unexpected hump can be observed at 60% of the passage on V_r and is slightly visible on V_θ. The wake RMS values are overestimated by all simulations at this radius, especially by LES1. The fan LE flow separation, which is already present at this radius in both LES, may actually be responsible for the larger RMS values observed in both LES with respect to the RANS. As a whole, the RMS profiles are sharper than the experimental ones and the background values are well captured.

At 50% rotor span (Fig. 20), the axial velocity deficit and the wake width are this time well captured by all the simulations. An overestimation of the background axial velocity is however observed. The background velocity is overestimated over almost the whole blade span, which indicates a mismatch between the HW and the performance measurements. The azimuthal velocity profiles are in good agreement with the experimental data especially for the two LES. The radial velocity is still over-predicted at this radial position, but is in better agreement with the experimental measurements than at 25% rotor span, especially for both LES, which give estimates that are closer to the measurements than the RANS does. These remaining discrepancies for the radial velocity component might be partially explained by the lack of accuracy of the experimental estimate using HWs, because comparable discrepancies have been observed on RANS studies on the ACAT1 fan stage (see Kissner et al. [48] for a comprehensive comparison of all available RANS simulations) and on other configurations [58]. As already mentioned about the 25% span results, the radial velocity is indeed very small compared with the two other components; therefore slight differences in the main components account for relatively large variations of the radial velocity. The wake RMS values are again overestimated by both LES for each component, whereas the RANS is able to recover both the background and the wake levels. A significant improvement in terms of absolute levels is however achieved with LES2. Furthermore, both LES results display profile shapes that faithfully reproduce those observed in the experiment, which is not the case for the RANS. This observation combined with the previously mentioned HW calibration issues, which may partly explain the larger difference between the LES and the measurements, support the fact that the LES approach better captures the underlying physics in the wakes than the RANS.

The significant blade-to-blade variations observed at 75% blade span (Fig. 21) result in a wide experimental revolution range. At this radial position, the RANS overestimates the axial velocity deficit whereas both LES are in fairly good agreement with the measurements. All the simulations recover quite well the experimental wake width but still overestimate the background values. The

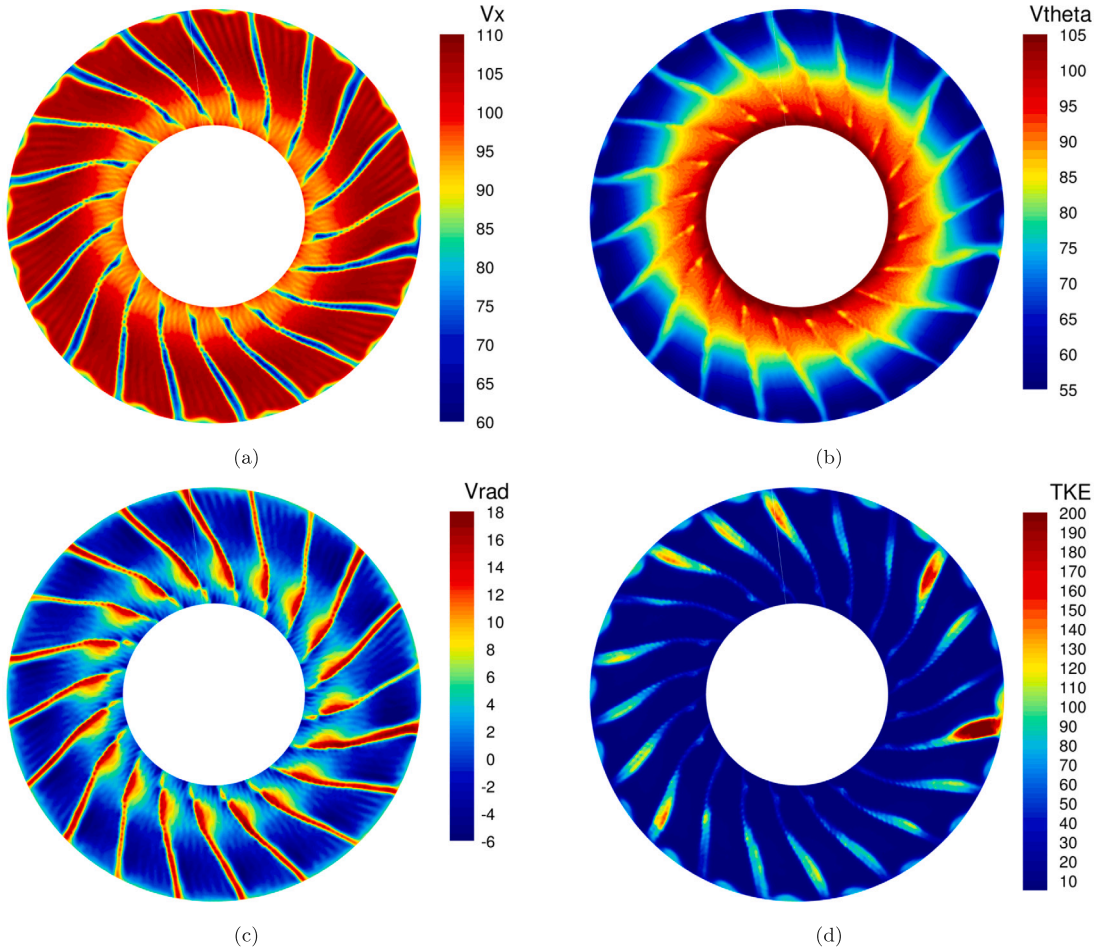

Fig. 18. Hot-wire measurements at position HW1. (a) Axial velocity, (b) Circumferential velocity, (c) Radial velocity, (d) Turbulence kinetic energy.

circumferential velocity profiles are in excellent agreement with the experimental data, especially LES2, which perfectly matches the experimental values. The RANS and LES1 slightly underestimate the background values. Regarding the radial velocity, an over-prediction can still be observed for all simulations, but it is considerably more pronounced for the RANS. On the contrary, the LES2 profile shows a better agreement with the experimental one than what has been observed at lower radial positions. Concerning the RMS profiles, similarly to what has been observed at 50% rotor span, both LES predict profiles with shapes faithfully reproducing the experimental ones, unlike the RANS. In terms of magnitude, the RANS recovers the axial RMS velocity but slightly overestimates the azimuthal and radial profiles. LES1 provides higher values for all three components, whereas LES2 is in good agreement with the HW measurements, with profiles that are almost entirely within the range of experimental values, confirming the significant improvements achieved by LES2.

The last radial position discussed herein, is located at 95% rotor span (Fig. 22). The largest discrepancies are found for the RANS simulation. Indeed, it significantly overestimates the axial velocity deficit as well as the magnitude of both the radial and the circumferential velocity components. Both LES, on the contrary, are in very good agreement with the measurements in terms of magnitude and shape for the axial and azimuthal velocity components, while the radial component is still overestimated. Important blade-to-blade variations are observed for the experimental RMS values, as indicated by the wide experimental revolution range. This makes the reading of the results more difficult but still shows that the shape of the profiles are better captured by the LES approach for all velocity components. In terms of magnitude, only LES2 recovers the experimental levels, as the LES2 profiles are all close to the upper limit of the experimental range. Both the RANS and LES1 tend to overestimate the RMS levels for all components.

To get an additional insight into the radial distribution of the mean flow velocity components across the duct channel, the radial profiles of each mean and RMS velocity component are provided in Fig. 23. Both axial and circumferential velocity components are in good agreement with the measurements for all simulations. Slight differences appear for the circumferential velocity close to the shroud and around 30% span. As already highlighted with the azimuthal profiles, the radial component of the velocity is overestimated especially between 10% and 70% of the duct channel height. Above 70% span, the largest discrepancies are

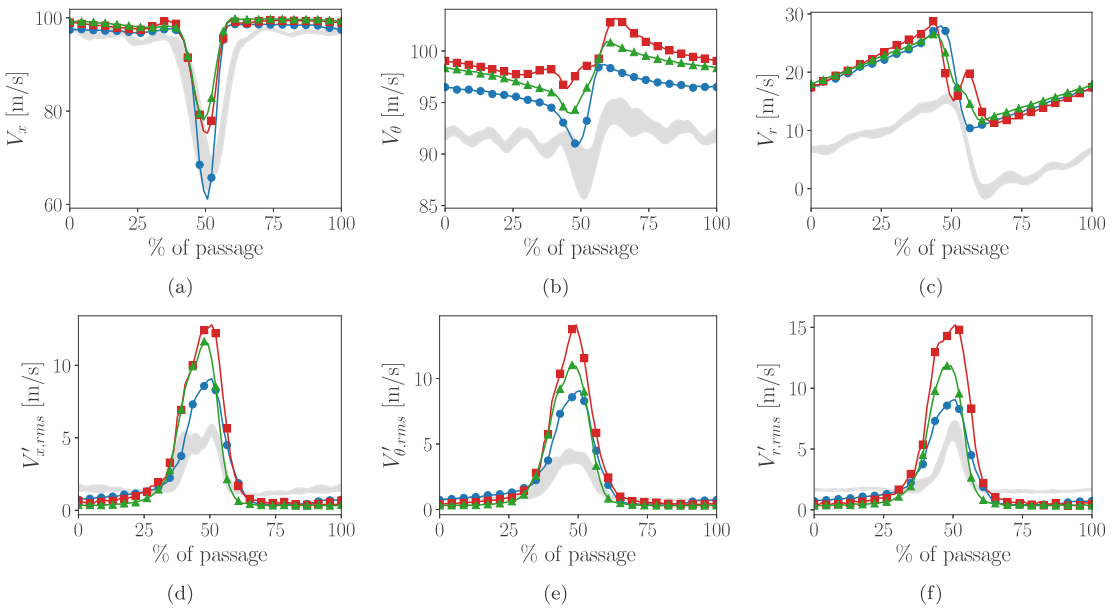

Fig. 19. Velocity component azimuthal profiles at 25% rotor span. Experimental revolution range( ), RANS ( ), LES1 ( ), LES2 ( ). (a) V_x, (b) V_θ, (c) V_r, (d) $V'_{x,rms}$, (e) $V'_{\theta,rms}$, (f) $V'_{r,rms}$.

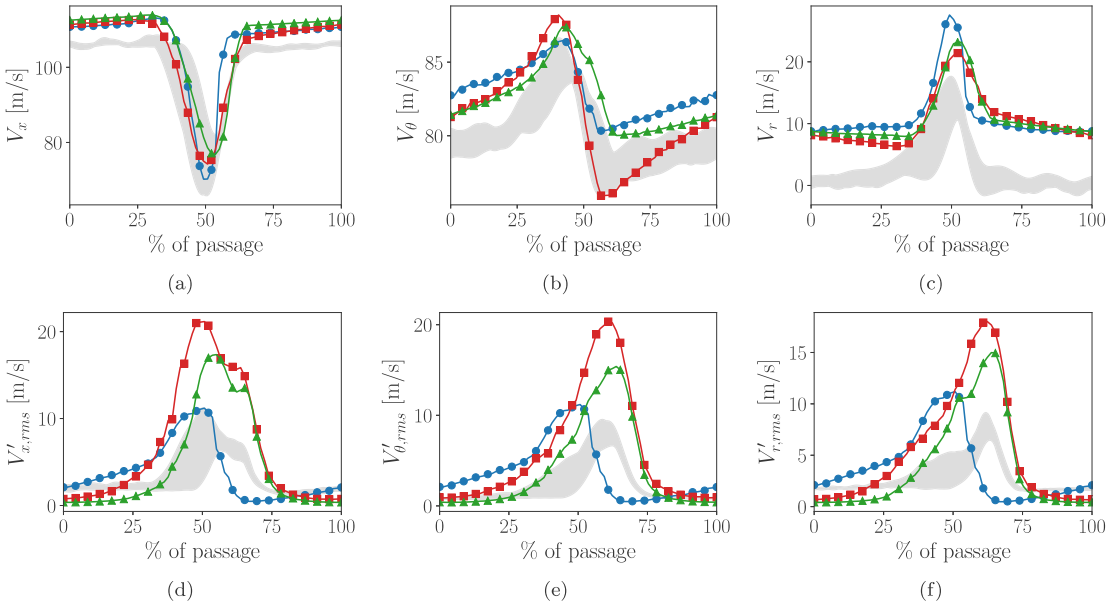

Fig. 20. Velocity component azimuthal profiles at 50% rotor span. Experimental revolution range( ), RANS ( ), LES1 ( ), LES2 ( ). (a) V_x, (b) V_θ, (c) V_r, (d) $V'_{x,rms}$, (e) $V'_{\theta,rms}$, (f) $V'_{r,rms}$.

observed with LES2 because the background value is overestimated in this region, even though the wake values are closer to the experiment compared with the other simulations. François et al. (Figure 12 in [23]) observed the same kind of disparities and confirmed an inconsistency in the measurement of the radial component of the velocity. They showed that the long gap configuration measurements at the HW1 position are indeed closer to the simulation results, while they should be similar to that of the short gap configuration as the potential effect of the OGV is not expected to have such an important effect on V_r. The shape of the RMS profiles is very similar to that of the measurements. The RMS levels predicted by LES1 are significantly overestimated for all components close to the hub and between 40% and 70% channel height. On the contrary, the RANS and LES2 profiles lie within the experimental revolution range. Again, the latter result confirms the improvements observed when using the refined mesh of LES2

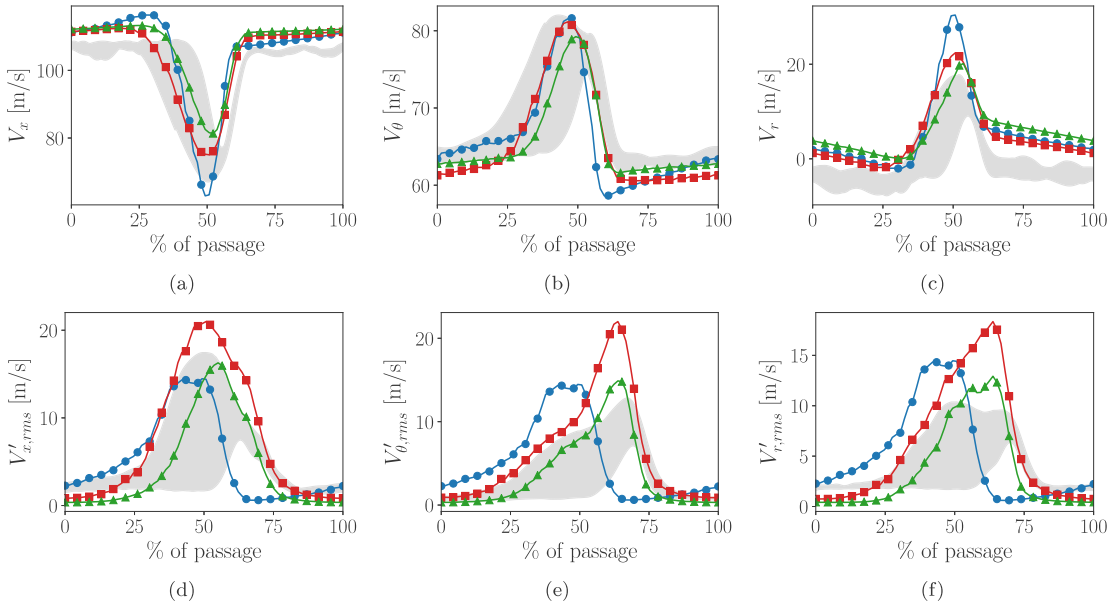

Fig. 21. Velocity component azimuthal profiles at 75% rotor span. Experimental revolution range( ), RANS (—●—), LES1 (—■—), LES2 (—▲—). (a) V_x, (b) V_θ, (c) V_r, (d) $V'_{x,rms}$, (e) $V'_{\theta,rms}$, (f) $V'_{r,rms}$.

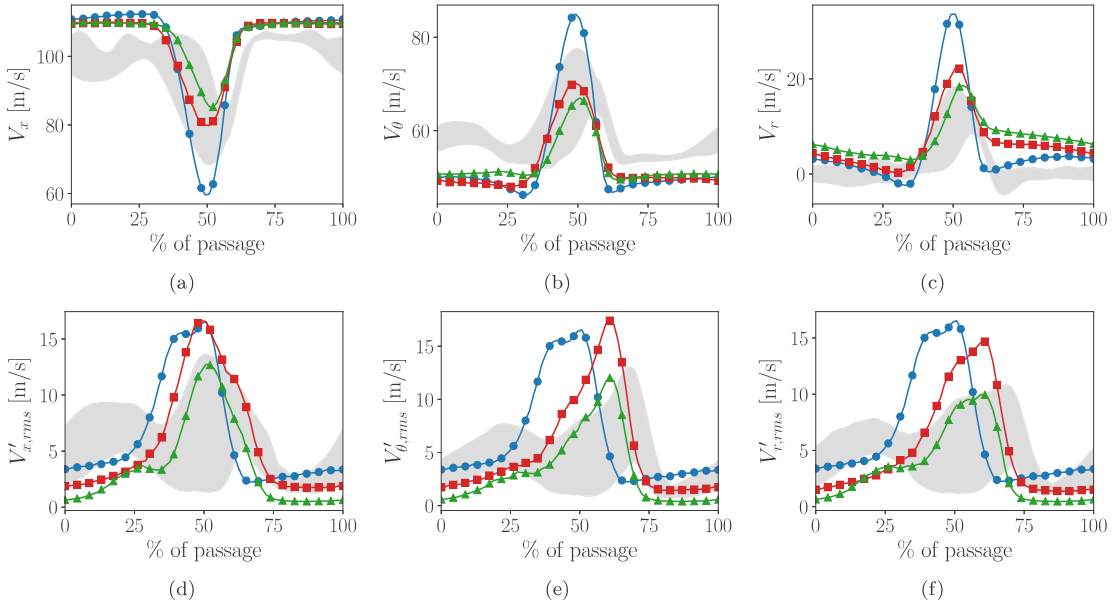

Fig. 22. Velocity component azimuthal profiles at 95% rotor span. Experimental revolution range( ), RANS (—●—), LES1 (—■—), LES2 (—▲—). (a) V_x, (b) V_θ, (c) V_r, (d) $V'_{x,rms}$, (e) $V'_{\theta,rms}$, (f) $V'_{r,rms}$.

As a concluding remark of this subsection, it should be underlined that since the hot wire is introduced from the casing, it is exposed to increasing lever forces as the support dives towards the casing: therefore vibrations that are expected to increase might affect the measured fluctuation levels. This might explain why the CFD results better match the experimental values near the casing as compared to the hub to mid-span region. Similarly, the rotor blades being attached to the hub, they experience stronger variations with increasing radial positions, which would explain the experimental revolution range increase towards the casing. Considering all these installation effects and the calibration uncertainties, the common trends of the 3 simulations and of the ZDES from François et al. [23] appear to be more consistent than the experimental values.

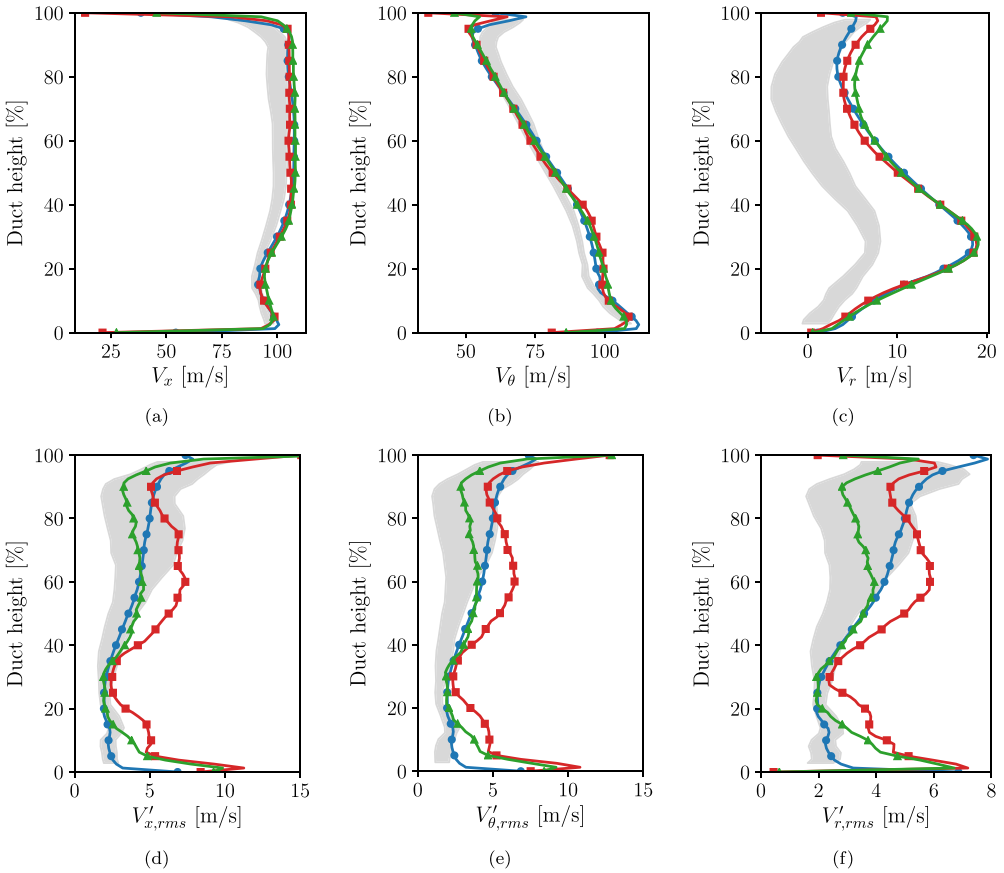

Fig. 23. Velocity component radial profiles at HW1 position. Experimental revolution range( ), RANS ( ), LES1 ( ), LES2 ( ). (a) V_x, (b) V_θ, (c) V_r, (d) $V'_{x,rms}$, (e) $V'_{\theta,rms}$, (f) $V'_{r,rms}$.

4.3.2. Velocity spectra

In order to obtain an insight into the turbulent energy distribution, the Power Spectral Density (PSD) of each velocity component at the HW1 position at 50% rotor span is displayed in Fig. 24. The simulation results are plotted along with the HW measurements at the same position. As already noticed in Section 4.3.1 when commenting the RMS levels, LES1 overestimates the PSD levels over the whole chosen frequency range and for all velocity components, whereas LES2 provides spectra that are much closer to the experimental data. More precisely, in Fig. 24(a), LES1 overestimates the axial velocity PSD by 5 to 10 dB between 1 kHz and 5 kHz while the overestimation for LES2 remains below 5 dB at low frequencies, and decreases down to 2 dB above 4 kHz. Above 5 kHz, the results of the two simulations overlay. The fact that higher PSD levels are observed at low frequencies for LES1 is actually consistent with the fact that larger coherent structures are observed in this simulation, compared with LES2. At about $7-8$ kHz, a sudden drop in the experimental PSD occurs, for all velocity components. A deeper analysis of the experimental data revealed that this drop actually results from the large diameter of the hot-wires: up to 12 μm were required to avoid failure during deep radial explorations, resulting in a cut-off frequency of about 8 kHz. This partly explains the fact that the RMS levels extracted from all the simulations are higher than the experimental values and that the computed spectra are not to be compared with the experimental ones above cut-off. Polacsek et al. [14] estimated that the measured RMS levels are underestimated by a factor of about 1.5 for all velocity components, that is, about −3.5 dB, which significantly reduces the overestimation observed in Section 4.3.1 for LES2. For the azimuthal velocity spectra, in Fig. 24(b), LES1 displays an almost constant gap of 10 dB from low frequencies up to the experimental cut-off frequency. LES2 provides more accurate results, with a gap of $1-2$ dB up to 3 kHz. Above this frequency, this gap progressively increases to reach a maximum value of 5 dB at 7 kHz. Above 7 kHz, the PSD levels retrieved from both simulations almost overlay. Finally, in Fig. 24(c), the LES1 radial velocity spectra are similar to the azimuthal spectra. The LES2 spectrum, on the contrary, is in very good agreement with the measurements with a discrepancy ranging from 1 dB at low frequency up to 3 dB near cut-off. Above cut-off (8 kHz), both simulation spectra overlay.

Note, however, that since the above correcting factor of 1.5 proposed by Polacsek et al. [14] was only estimated at two isolated radial positions (50% and 90% rotor span), assuming that this factor is constant over the entire blade span might be excessive. For the sake of completeness, comparisons of the present results with the corrected experimental data are plotted in Fig. 25, at 50% rotor span, along with the results obtained by François et al. [23] at the same radius. LES2 results are indeed much closer to these

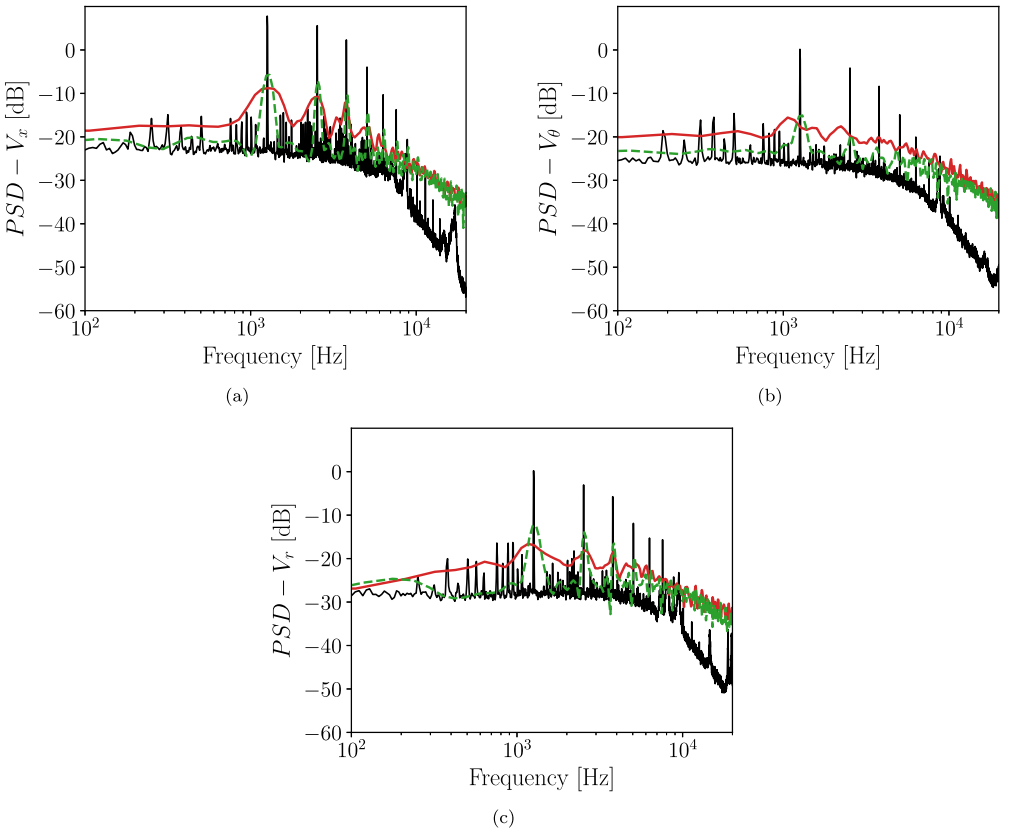

Fig. 24. PSD of the fluctuations of each velocity component at the HW1 position, at 50% rotor span. Experiment (——), LES1 (——), LES2 (- - -). (a) V_x, (b) V_θ, (c) V_r.

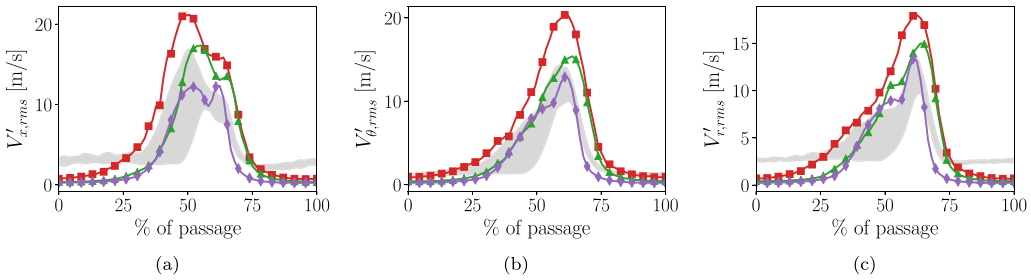

Fig. 25. Velocity component azimuthal profiles at 50% rotor span. Experimental revolution range( ) corrected with a 1.5 factor, LES1 (——), LES2 (——), ONERA ZDES (——). (a) V_x, (b) V_θ, (c) V_r, (d) $V'_{x,rms}$, (e) $V'_{\theta,rms}$, (f) $V'_{r,rms}$.

corrected experimental profiles, both in terms of shape and levels. François et al. [23] better recover the RMS levels, with curves within the experimental revolution range. However, the $V'_{x,rms}$ profile in their study exhibits a secondary peak that does not appear in the experiment.

4.4. Blade-to-blade instantaneous flow

Fig. 26 shows the instantaneous Mach number field at different radial positions for both LES. For all radial positions, the LES1 wake abruptly grows at the transition from the rotor to the stator domain. This is due to the coarser mesh in the downstream region, which enhances diffusion. This was not shown by the mean solution since the wakes vanish because of the averaging process. This phenomena is not observed anymore in LES2 thanks to its much finer mesh, except at 25% rotor span because the inter-stage refinement block does not extend down to the core flow region.

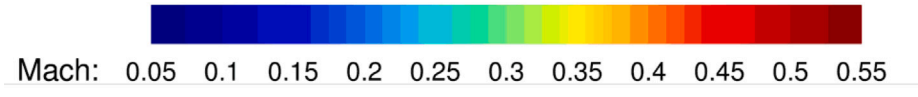

(a) LES1 - 25% rotor span.

(b) LES2 - 25% rotor span.

(c) LES1 - 50% rotor span.

(d) LES2 - 50% rotor span.

(e) LES1 - 75% rotor span.

(f) LES2 - 75% rotor span.

(g) LES1 - 95% rotor span.

(h) LES2 - 95% rotor span.

Fig. 26. Instantaneous Mach number field at different duct heights for both LES.

At 25% rotor span, the flow is very similar in the two simulations, except that the LES2 rotor wakes are thinner than those of LES1.

Above 25% rotor span, the turbulent nature of the flow can be clearly observed in both simulations. The flow is laminar on the rotor pressure side while a thick turbulent boundary layer develops on its suction side. The previously analyzed rotor LE flow detachment, which is partly responsible for this laminar-turbulent transition, has an intermittent behavior that results in the formation of vortices that graze along the blade suction side, and eventually feed the downstream wake. Al Am et al. [54] provided an in depth analysis of this phenomenon using a wall-resolved LES approach on a radial slice of a fan-OGV stage operating at approach conditions. Even though the limited span of the computation inevitably neglected part of the 3D phenomena occurring within a full-span configuration, Al Am et al. [54] were able to demonstrate that the state of the blade boundary layer, and of the subsequent wake, directly depend on the presence and size of the LE separation bubble they observed: the lower the mass-flow rate is, the thicker and more turbulent the boundary layer and wake are. Depending of the radial position, several differences can be observed in the stator domain between the two LES. At 50% rotor span, the flow detachment that occurs on the stator suction side in LES1 triggers an intense vortex shedding at the trailing edge. This is not observed in LES2 except at 75% rotor span for which a much less intense vortex shedding is observed. Moreover, in both LES, the influence of the rotor wakes onto the boundary layer development and the wakes of the impacted stator vanes is found to be significant at 75% and 95% span. As a result of the 20/40 blade/vane count, this influence affects half of the vanes at the same time and consists in thickening the boundary layers and wakes. It is more pronounced at 95% span and hardly identifiable at 50% span. Finally, at 95% rotor span, the tip gap flow is also well captured by LES2 and slightly dissipated by LES1. It directly interacts with the wake of the neighboring blade, at its trailing edge.

5. Acoustic analysis

5.1. Noise sources overview

Radiated noise is predicted by feeding rotor and stator wall pressure fluctuations into the Ffowcs Williams and Hawkings or the Goldstein analogy. Assumptions are made neither on the blade and vane geometries (thickness, camber, stagger angle, sweep) nor on the flow conditions (flow angle, viscosity, load, isotropic turbulence). Therefore the prediction takes into account all the simulated broadband noise sources of the two blade rows. In particular, since the compressibility of the unsteady highly resolved simulation inherently takes into account the scattering by the blades and vanes of the sound generated in its vicinity, determining the Green's function of the blades and vanes is not required. Nonetheless, cascade effects are only partially taken into account as the mutual influence is limited to a varying number of neighboring blades depending on the grid resolution for a given discretization scheme. Before performing any noise predictions, it is thus of prime interest to analyze the broadband noise sources on the blade and vane surfaces. A practical way to get an overview of the potential noise sources is to examine the root mean square of the pressure fluctuations on the surfaces of interest. Fig. 27 shows the P_{rms} on the stator surface. For both LES, high levels of P_{rms} can be observed at the stator leading edge. This expected phenomenon is typical of the RSI mechanism and results from the impact of the turbulent rotor wakes onto the stator. The LES2-RMS levels at the stator LE are remarkably lower than those of LES1, indicating a weaker rotor–stator interaction. Another explanation could be that the LES1 turbulent wakes contain more large scale structures than those of LES2: these are undergoing stronger distortions as they hit the vane leading edge and are thus radiating more efficiently. A second zone of high RMS levels, starting at about 60% stator chord, can be observed in both LES. This zone corresponds to the boundary layer transition observed in Section 4.2.1. Higher RMS levels are found in this zone in LES1, since the turbulent transition is much sharper due to the boundary layer separation. Given that the rear-part pressure fluctuations are not negligible with respect to the leading edge ones and that they occur not too far from the trailing edge, they may contribute to some extent to the total radiated noise.

Regarding the fan sources, Fig. 28 reveals that significant RMS levels can be observed at the same location as the rotor leading edge vortex. The magnitude of the fluctuations in both LES is similar and comparable to those at the stator leading edge. As a consequence, depending on the efficiency of the radiation process, this source may significantly contribute to the total radiated noise. These two latter points will be investigated more precisely in the next section.

In order to have a better idea of the frequency content of these fluctuations, the PSD of the pressure fluctuations ϕ_{pp} has been computed along the chord of the stator and of the rotor at 50% stator span and 75% rotor span, respectively. For the stator (see Fig. 29), the leading edge pressure fluctuations are spread over the whole frequency range, with higher values from 1 to 10 kHz in both simulations. As already mentioned, the LES2 ϕ_{pp} values are slightly lower at this position than those of LES1. The pressure fluctuations in the rear-part of the OGV (60% to 100% of the stator chord) are the most intense between 1 and 8 kHz for both simulations: they are the footprints of a wide range of turbulent structures of different sizes that are generated in the downstream part of the vane. As suggested by the RMS values, the ϕ_{pp} levels are 10 dB higher in LES1 than in LES2, indicating a much stronger boundary layer transition. For both simulations, intense ϕ_{pp} levels are observed at the BPF and its harmonics over the whole vane chord because of the convection of the rotor wakes throughout the inter-vane channel. In LES1, the lower sampling frequency of the signal as well as the lower mesh resolution lead to a wide zone of low ϕ_{pp} magnitude at high frequency, which disappears in LES2. A similar zone can also be observed in the case of the rotor (see Fig. 30). The LES1 and LES2 ϕ_{pp} maps on the rotor are relatively similar: the highest levels are observed near the leading edge where the vortex occurs, and are spread over a significant part of the chosen frequency range as the first noticeable decrease in ϕ_{pp} starts at around 10 kHz. The boundary layer transition resulting from the flow separation creates significant pressure fluctuations between 1 and 10 kHz over the entire blade chord, which once again

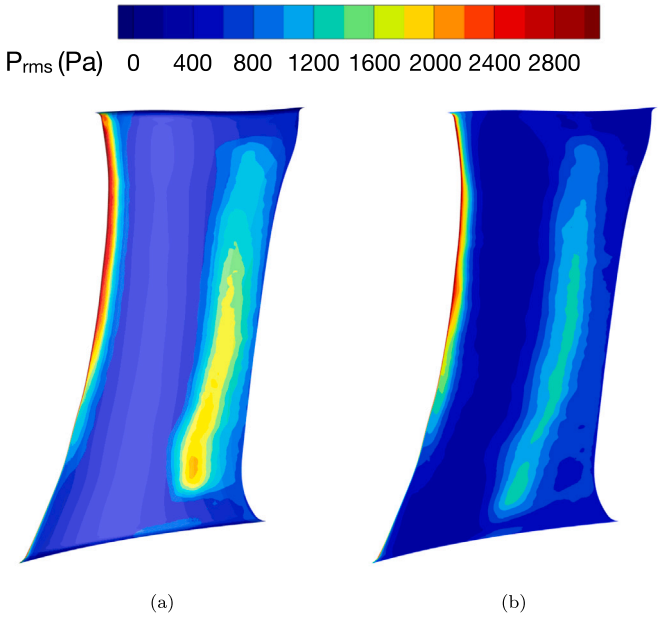

Fig. 27. P_{rms} values on the stator suction side. (a) LES1, (b) LES2.

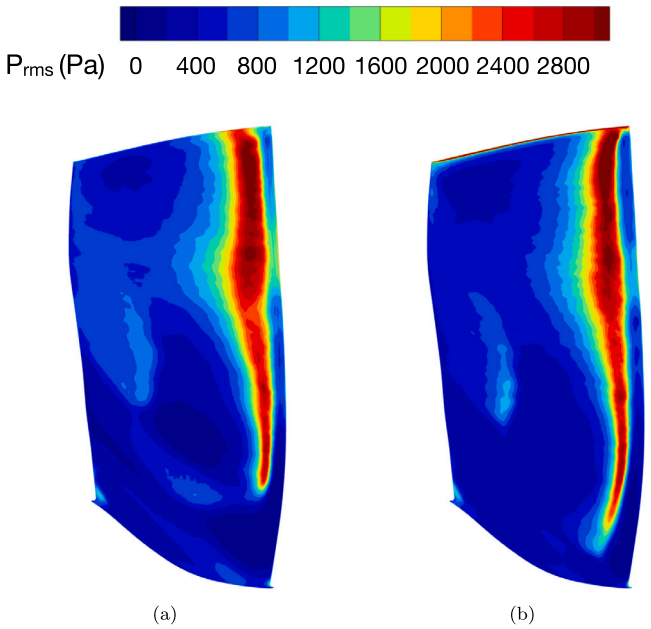

Fig. 28. P_{rms} values on the rotor suction side. (a) LES1, (b) LES2.

is a footprint of the wide range of turbulent structures of different sizes that develop over the blade. In both simulations, a global decrease in ϕ_{pp} by 10 to 15 dB is observed from the leading edge down to the trailing edge.

All these observations confirm that, apart from the RSI mechanism, other broadband noise sources, which are mainly related to flow separations and boundary layer transitions, can be identified in the ACAT1 fan stage at approach conditions. Furthermore, the order of magnitude of the pressure fluctuations associated with these sources is comparable to that of the RSI mechanism, which may significantly contribute to the total radiated noise. Polacsek et al. [24] obtained RSI sources of similar order of magnitude using a ZDES approach. They also highlighted the presence of secondary noise sources on the OGV. They observed local flow detachments close to the OGV TE, resulting in pressure fluctuations with a magnitude lower than that obtained in the present study. Their analysis of the streak lines and the P_{rms} on the OGV (Figure 13 in [24]) also revealed local flow detachments at the OGV LE that tends to

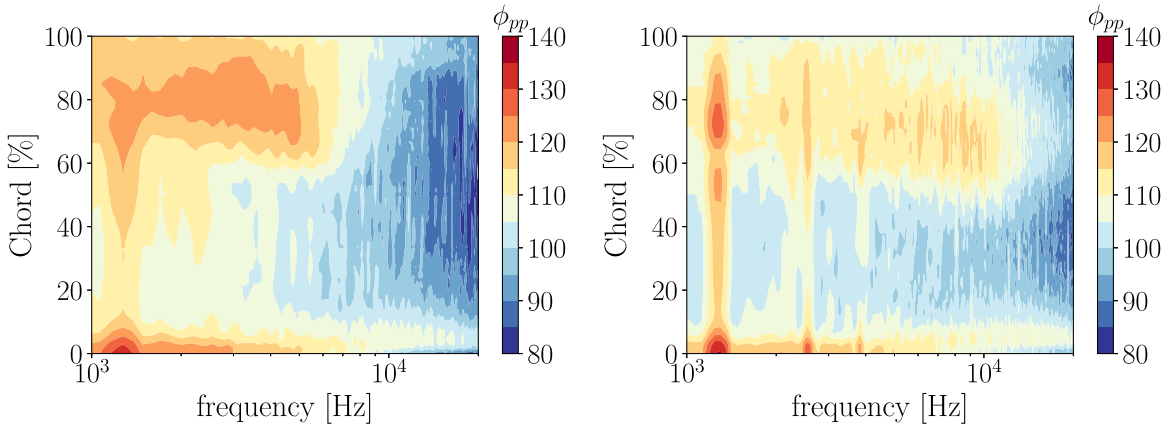

(a) LES1 (10 windows). (b) LES2 (5 windows).

Fig. 29. PSD of the pressure fluctuations on the stator surface at 50% stator span. Units in dB, $P_{ref} = 2.10^{-5}$ Pa.

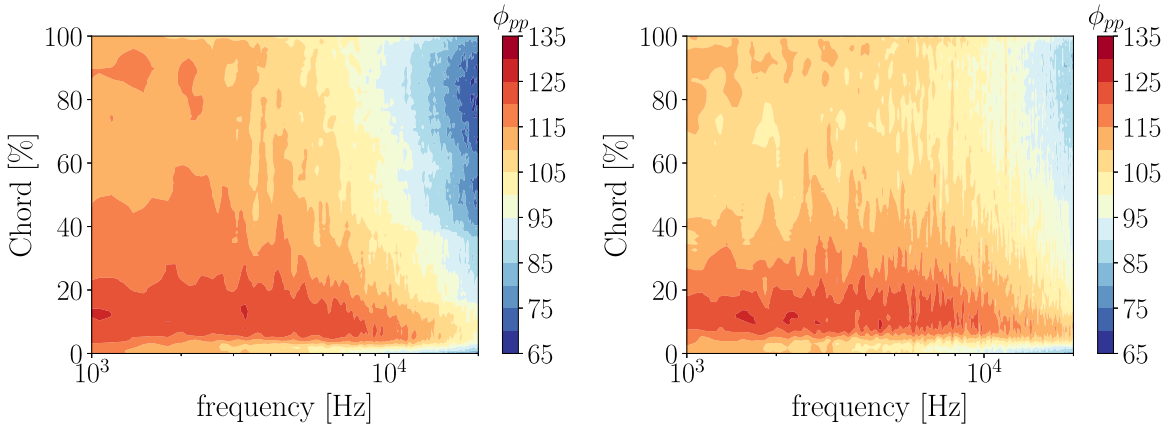

(a) LES1 (10 windows). (b) LES2 (5 windows).

Fig. 30. PSD of the pressure fluctuations on the rotor surface at 75% fan span. Units in dB, $P_{ref} = 2.10^{-5}$ Pa.

blend with the RSI source. Indeed, as in the present study, the P_{rms} level associated to RSI sources usually steadily increases along the OGV span, roughly following the radial evolution of the rotor wake TKE (as also shown by Al Am et al. [59]), which is the driving mechanism of the RSI noise. Polacsek et al. [24], on the contrary, observe a uniform area of high P_{rms} levels at the LE, over the entire OGV span, which may behave as an additional LE noise source. This is however absent from the present LES.

5.2. RSI mechanism

5.2.1. Incident flow

Another essential property to investigate is the coherence function, which measures the correlation of two signals as a function of their frequency and is defined as the normalized cross-spectrum of the two signals. Here it is applied to two-point recording of single velocity components. As the frequency of the turbulence can be related to the size of its structures, the coherence function can be interpreted as the correlation of the turbulent structures in a chosen direction with respect to their size. The coherence function of the velocity component u_i at two points (x, θ, r) and (x', θ', r') can be expressed as follows:

$$\gamma^2_{u_i}\left(x,\theta,r,x',\theta',r',\omega\right) = \frac{\left|\boldsymbol{\Phi}_{u_i}\left(x,\theta,r,x',\theta',r',\omega\right)\right|^2}{\boldsymbol{\Phi}_{u_i}(x,\theta,r,\omega)\boldsymbol{\Phi}_{u_i}\left(x',\theta',r',\omega\right)}, \tag{3}$$

where $\boldsymbol{\Phi}_{u_i}\left(x,\theta,r,x',\theta',r',\omega\right)$ is the cross power spectral density of the velocity component u_i and $\boldsymbol{\Phi}_{u_i}(x,\theta,r,\omega)$ is the power spectral density of the same velocity component at the point (x, r, θ). In the present case, the data have been extracted from both LES at the LE1 position (shown in Fig. 2) along a selected radius so that θ and x remain constant when r' is varied along the radius. The

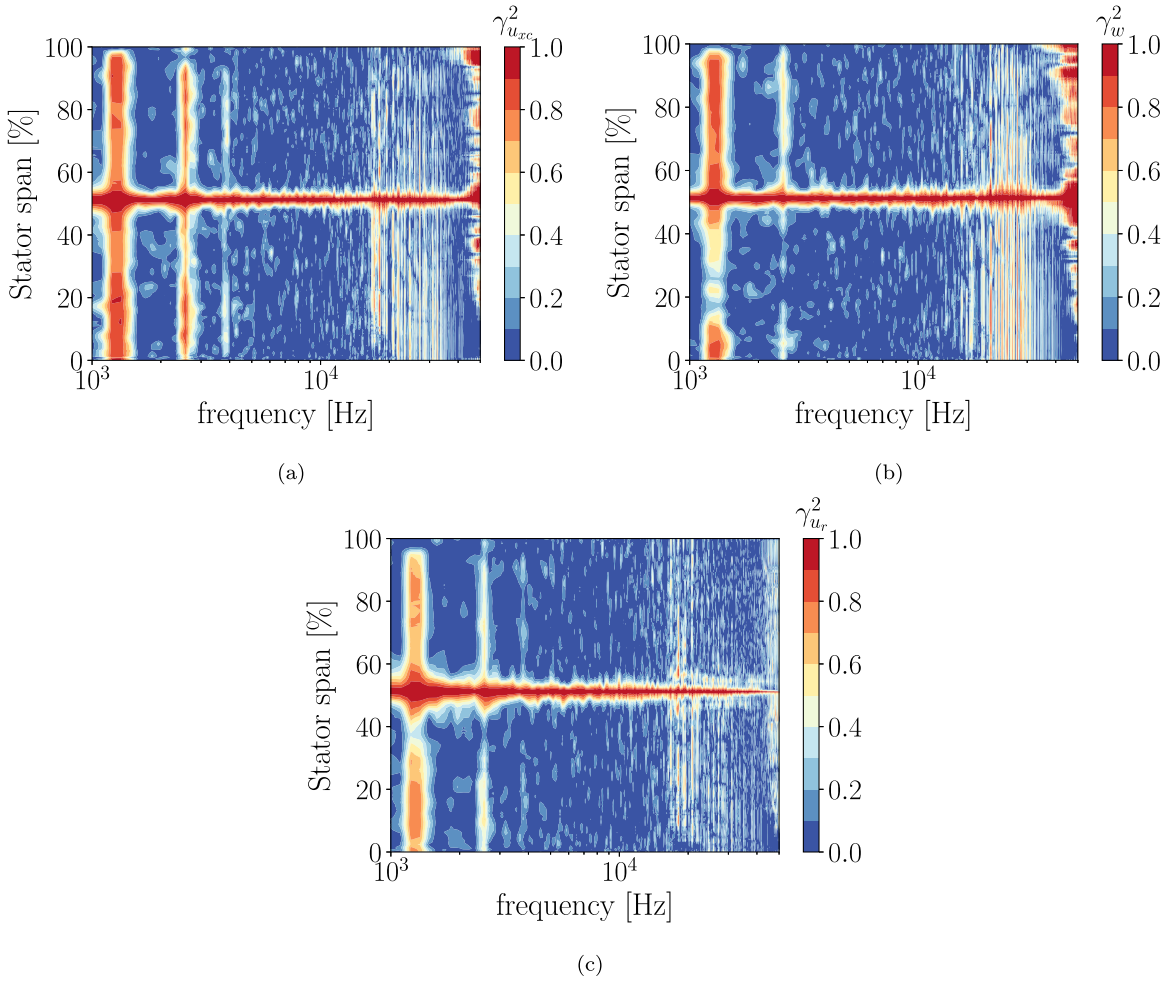

Fig. 31. LES1 radial coherence function contours for each velocity component in the cascade frame of reference. Reference radius at stator midspan (10 windows). (a) u_{xc}, (b) w, (c) u_r.

coherence function thus not only depends on the separation $r' - r$ between the two points, but also on their position relative to the blade, that is, the radial position r, since the flow is not homogeneous and x, θ are fixed. The coherence function thus becomes a radial coherence function and can be rewritten $\gamma^2_{u_i}(r, r', \omega)$. Figs. 31 and 32 show the radial coherence as a function of the frequency and the radius r' for LES1 and LES2, respectively. In the present study, the coherence function has been plotted for the velocity component in the cascade reference frame, the reference radius r being located at midspan. u_{xc}, w and u_r correspond to the velocity along the vane chord, the upwash velocity (normal to the chord) and the radial velocity, respectively. They have been computed assuming that the geometric chord of the real vane is equal to the chord of the equivalent flat plate.

At midspan, the coherence is equal to 1 for all the velocity components since the two points (x, θ, r) and (x, θ, r') coincide and the cross power spectral density becomes a PSD. For LES1, some interferences, which are mainly due to the sampling frequency and to the mesh resolution, appear at high frequencies. They almost disappear in the LES2 coherence maps. The shorter LES2 signals, however, induce a higher statistical background coherence noise. For both LES and for all velocity components, significant coherence values are observed at the BPF and its harmonics since the periodic part of the velocity signals has not been removed. The first two BPF harmonics are observable for u_{xc}, while only the first harmonic is captured for the two other components. This suggests that the source related to the second harmonic (3 BPF) might be less efficient than the first harmonic as it barely contributes to the upwash velocity coherence. Apart from these isolated frequencies, for both LES and for all the velocity components, the coherence quickly decreases, which means that the turbulent structures share equivalent properties in the three directions. The radial extent over which the turbulent structures are correlated seems to be similar for all the velocity components. This is confirmed by Fig. 33, which shows the evolution of the radial coherence length scale, defined in Eq. (4), for each velocity component with respect to the frequency. Each simulation shows a mean radial coherence length scale equivalent to 5–10% of the stator span for all the velocity components, which is less than the 20% of the stator span observed by de Laborderie et al. [60] in their study on the CME2 low

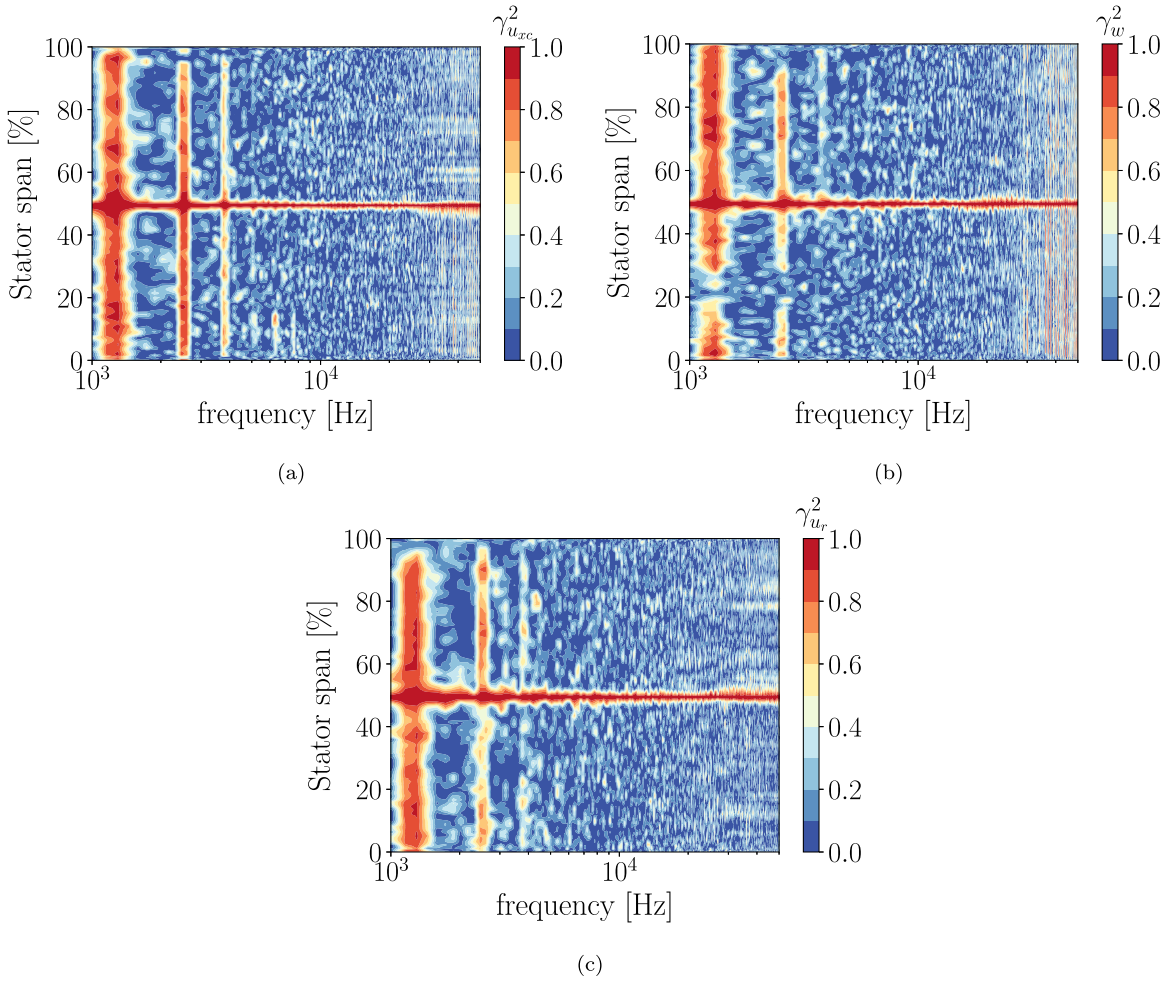

Fig. 32. LES2 radial coherence function contours for each velocity component in the cascade frame of reference. Reference radius at stator midspan (5 windows). (a) u_{xc}, (b) w, (c) u_r.

pressure compressor.

$$L_{r,u_i}(\omega) = \int_{R_H}^{R_T} \sqrt{\gamma^2_{u_i}(r, r', \omega)}\mathrm{d}r' \tag{4}$$

The high level of background noise observed in Figs. 31 and 32 is associated with the limited signal duration and a limited number of sampling locations. Hence the integration in Eq. (4) performed on the raw coherence maps would yield a nonphysical overestimation of the coherence length given the slow convergence of such a statistical estimator. To alleviate this problem, for each frequency, the correlation values above a threshold of 0.25 are approximated by a Gaussian function before integration. This adhoc approach appears to provide results in agreement with Polacsek et al.'s [24] estimate of the radial coherence lengthscale. This procedure still provides nonphysical estimation above a frequency of 15 kHz. A better estimation could possibly be obtained with longer time signals and advanced modal decomposition such as iterative Bayesian inverse approach [61].

5.2.2. Vane response

Similarly to the analysis made on the incident flow, it is of great interest to study the radial or spanwise coherence of the vane response to the RSI mechanism. To do so, the coherence of the pressure on the vane surface γ_p has been computed for both LES, at 0.5% vane chord over the whole stator span (see Fig. 34). As with the velocity components, the midspan position has been chosen as the reference location, which explains the high coherence value at 50% stator span. From this position, γ_p quickly decreases in both simulations except at the BPF and its harmonics, as with the coherence of the velocity components. This indicates that the radial extent over which the vane response is correlated is limited with respect to the stator span. This is confirmed by Fig. 35, which shows the evolution of the radial coherence length scale of the pressure fluctuations $L_{r,p}$ on the stator suction side at 0.5% stator chord over the whole vane span. As with the impinging flow, the background noise in Fig. 34 is quite significant and would

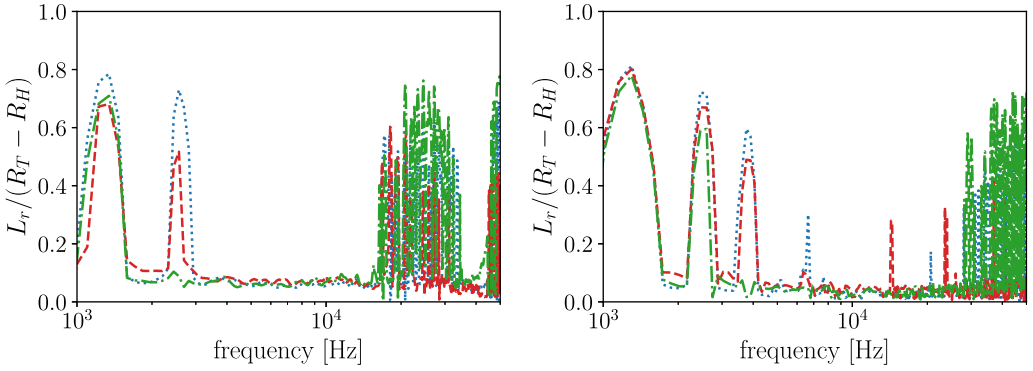

Fig. 33. Radial coherence length scale for each velocity component. $L_{r,u_{xc}}$ (·····), L_{r,u_r} (– – –), $L_{r,w}$ (– · –). (a) LES1, (b) LES2.

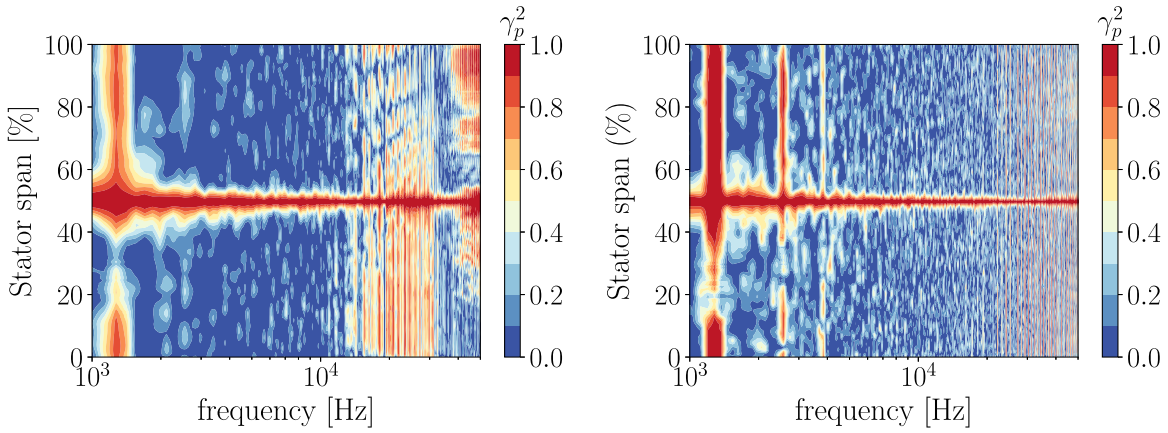

(a) LES1 (10 windows). (b) LES2 (5 windows).

Fig. 34. Radial coherence function contours of the pressure fluctuations on the stator vane suction side at 0.5% stator chord. Reference radius at stator midspan.

artificially increase the $L_{r,p}$ estimate. Hence the same filtering procedure as with the velocity components is applied before the spacial integration. In both simulations, $L_{r,p}$ is of the same order of magnitude as the radial coherence length scale of all velocity components. This is actually consistent with the hypothesis made in Posson's model [62], which considers that the cross-spectral density of the pressure jump on the vane is negligible above a certain radial coherence length scale, which is chosen to be equal to the radial coherence length scale of the incident upwash velocity. The validity of this hypothesis seems to depend on the considered configuration since De Laborderie [63] found that the coherence length scale of the vane response can be 3 to 4 times larger than that of the upwash velocity in a low pressure compressor.

5.3. Noise predictions

A hybrid numerical approach has been used to estimate the broadband noise radiated by the ACAT1 stage. As previously explained, this kind of method is a two-step approach in the spirit of acoustic analogies: determine the sources in the first step and propagate them to the receiver in a second step using a specific solver or analytical model. In the research presented here, the acoustic sources are computed from the scale-resolving flow simulations LES1 and LES2 and propagated to the observer using convolutional acoustic analogies. More precisely, the sources correspond to the wall-pressure fluctuations on the stator and on the rotor surfaces, which have been extracted from the simulation over about 4.5 and 3 rotations for LES1 and LES2, respectively. These pressure fluctuations are fed into the dipole terms of Ffowcs Williams and Hawkings' free-field analogy and the extension of Goldstein's analogy to annular duct [7] (Eq. (3.6), p. 116 applied to annular ducts). Both analogies are implemented in the tools *SherFWH* and *SherGoldstein* developed by the Aeroacoustics Group of Université de Sherbrooke [12,64]. *SherFWH* is an implementation of the formulations of Casalino [65] and Najafi-Yazdi et al. [66]. SherGoldstein computes the acoustic power in the upstream and downstream directions according to Eq. (5a) from [62], which makes direct use of the pressure amplitude of each annular duct mode resulting from the Fourier transform of the pressure jump through the blade/vane. Further details about these tools are provided

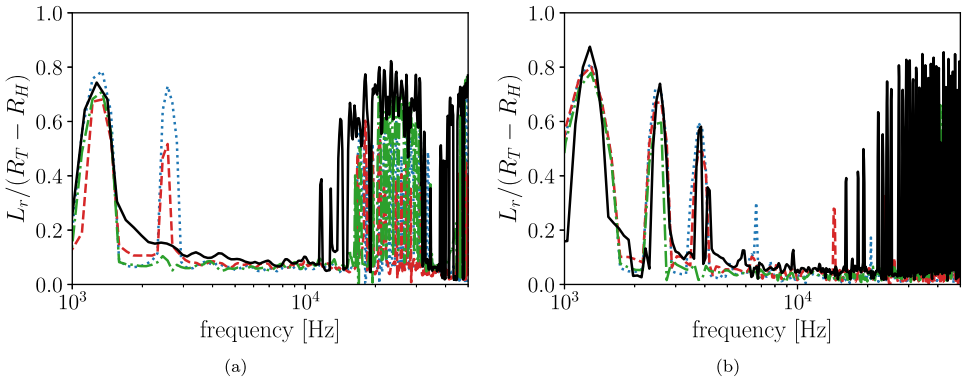

Fig. 35. Radial coherence length scale for each velocity component and for the pressure fluctuations at the stator leading edge. $L_{r,u_{xc}}$ (·····), L_{r,u_r} (- - -), $L_{r,w}$ (- · - · -), $L_{r,p}$ (——). (a) LES1, (b) LES2.

in [12]. As already mentioned, the FW-H analogy propagates the sound in free-field, which means that high-pass mode filtering due to the duct geometry is neglected, contrary to Goldstein's analogy. Both analogies neglect the noise shielding induced by the presence of the rotor and stator rows. Moreover, extracting the sources directly on the vane/rotor surface implies that the quadrupole sources, related to the volume term of the FW-H analogy [67], are neglected. This is actually a fairly reasonable assumption since the relative tip Mach number of the rotor is of 0.57, which makes it possible to neglect both monopole and quadrupole sources [67].

5.3.1. Stator noise

Fig. 36 shows the predictions obtained with both FW-H's and Goldstein's analogies based only on the stator sources retrieved from LES2. Similarly to what Lewis et al. [17] observed with the LES1 predictions, the shape of both the upstream and the downstream experimental noise spectra is faithfully recovered by the FW-H predictions. Nevertheless, the absolute levels are still overestimated, especially in the upstream direction for which there is a 5 to 7 dB gap with the experiment between 1 kHz and 5 kHz. In the downstream direction, this low-to-mid frequency gap does not exceed 5 dB. Above 5 kHz, however, an almost constant gap of 4 dB in the upstream direction, and of 2 dB in the downstream direction are observed. Despite this overprediction, the LES2 FW-H noise estimates are in much better agreement with the experimental spectra than the LES1 predictions (see Fig. 37). For both the upstream and the downstream predictions, the gap with the experiment from low to medium frequencies is still present but has been reduced by almost 5 dB. This leads to a downstream prediction that almost recovers the low frequency experimental noise levels, which is consistent with the shrinking of the wake turbulent structures observed in Section 4.4 for LES2 with respect to LES1. For frequencies above 5 kHz, however, only little improvement is observed since the predictions of both LES almost overlay.

Taking into account the duct cut-off effect on propagation further improves the noise estimates. Goldstein's analogy indeed provides noise levels that are at least 2 dB lower than those obtained with FW-H's analogy over the entire chosen frequency range, while still recovering the experimental spectrum shape. A higher noise reduction of about 5 dB can even be observed between 3 kHz and 6 kHz. This substantially reduces the overprediction compared with the free field analogy, confirming that neglecting the duct cut-off effect is partly responsible for it. This reduction, though consistent with what Pérez Arroyo et al. [12] observed, is less significant than that observed by Lewis et al. [17], when comparing the predictions obtained with both analogies using the LES1 data (see Fig. 38). This may stem from the fact that the larger turbulent structures in the LES1 most likely created more low-frequency acoustic duct modes, which are typically those that are cut-off by Goldstein's analogy. Since these acoustic modes are less present in LES2, the low-frequency noise reduction obtained with Goldstein's analogy is expected to be smaller. This leads to a reduced gap between LES1 and LES2 Goldstein predictions with respect to that observed with the FW-H analogy (see Fig. 39).

Regardless of the chosen acoustic analogy, the LES2 predictions are overall in much better agreement with the experiment than the LES1 predictions, which suggests that a mesh as fine as that of LES2 is mandatory to provide reliable results using this approach. The finer LES2 mesh indeed enabled to better capture wall flow phenomena and accurately transport the turbulent structures they generated. As highlighted in Section 5.1, this resulted in a significant modification of the noise sources in terms of position, magnitude and frequency range of interest. In order to assess to which extent this affected the noise contribution of each source on the stator, the latter was divided into two parts: the front part, consisting of the first 40% of the vane maximum axial chord over the entire vane span, and the aft part, which consists of the 60% left. The front part mainly encompasses the RSI sources whereas the aft one corresponds to the location of the separated zone in LES1. Such a splitting was also performed by Lewis et al. [17] on the LES1. Considering this splitting, the PSD Φ_{Full} induced by the pressure fluctuations over the full vane at a particular observer point can be rewritten as follows:

$$\Phi_{Full} = \Phi_{Front} + \Phi_{Aft} + 2Re(\Phi_{Front,Aft}), \tag{5}$$

where Φ_{Front} and Φ_{Aft} are the PSD induced by the front and the aft parts of the vane, respectively, $\Phi_{Front,Aft}$ is the cross-spectral density between the front and the aft parts, and $Re()$ denotes the real part of the quantity in parentheses. These three terms

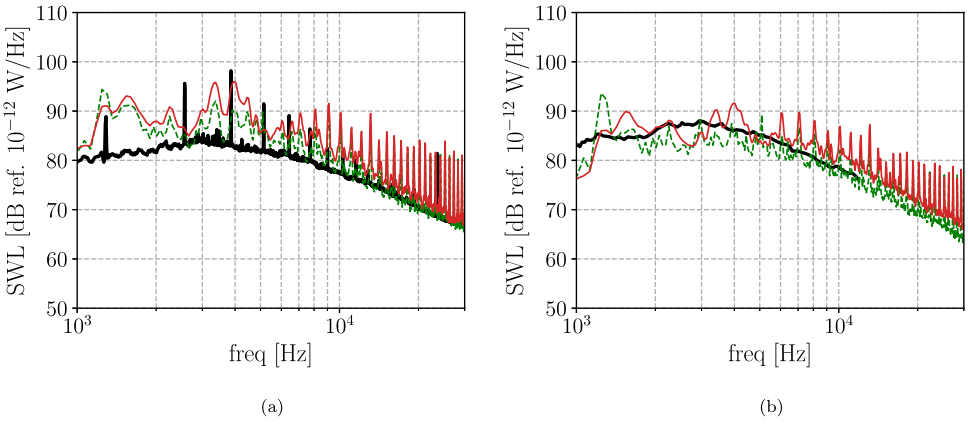

Fig. 36. Comparison of the LES2 Upstream SWL (left) and downstream SWL (right) spectra obtained from Ffowcs Williams and Hawkings' and Goldstein's analogies (5 windows). Experiment (——), FW-H (——), Goldstein (- - -).

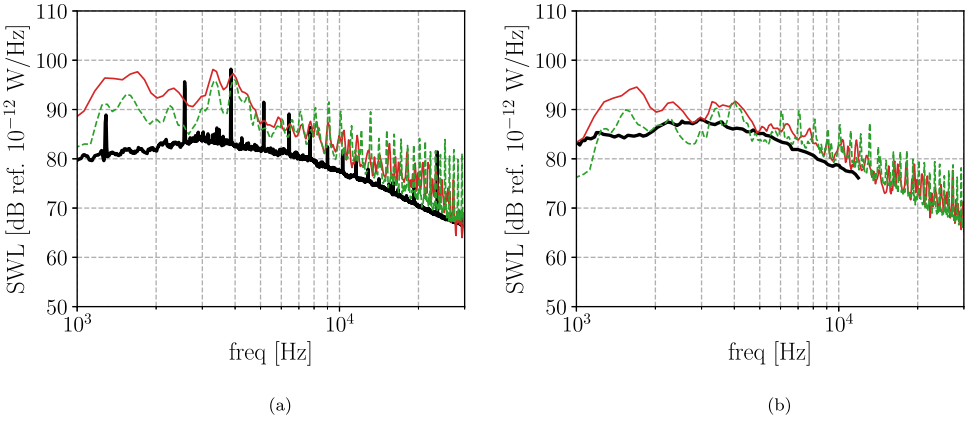

Fig. 37. Upstream SWL (left) and downstream SWL (right) spectra obtained from Ffowcs Williams and Hawkings' analogy (LES1: 10 windows, LES2: 5 windows). Experiment (——), LES1 (——), LES2 (- - -).

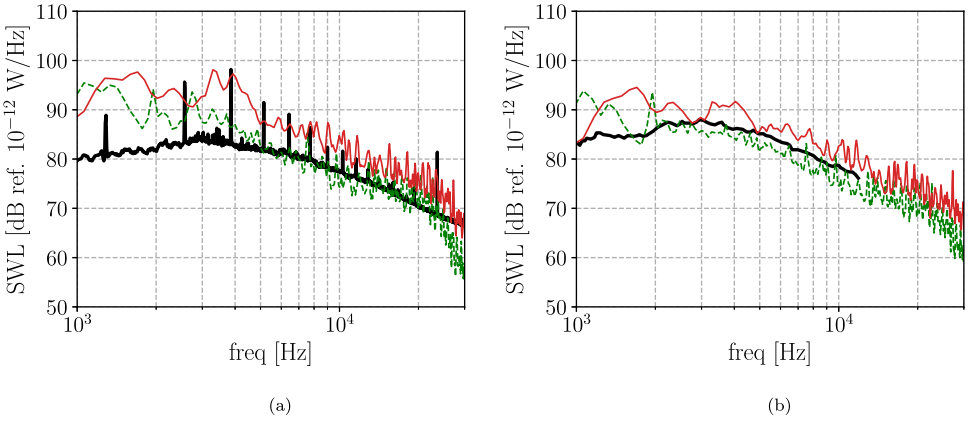

Fig. 38. Comparison of the LES1 Upstream SWL (left) and downstream SWL (right) spectra obtained from Ffowcs Williams and Hawkings' and Goldstein's analogies (10 windows). Experiment (——), FW-H (——), Goldstein (- - -).

(Φ_{Front}, Φ_{Aft}, and $2Re(\Phi_{Front,Aft})$) are plotted along with the full-vane based FW-H prediction in Figs. 40 and 41 for LES1 and LES2, respectively. The absolute noise levels of each sub-part contribution are significantly higher in LES1 than in LES2. However, their relative contributions with respect to the total stator noise is fairly the same in both simulations. The aft part remains the most

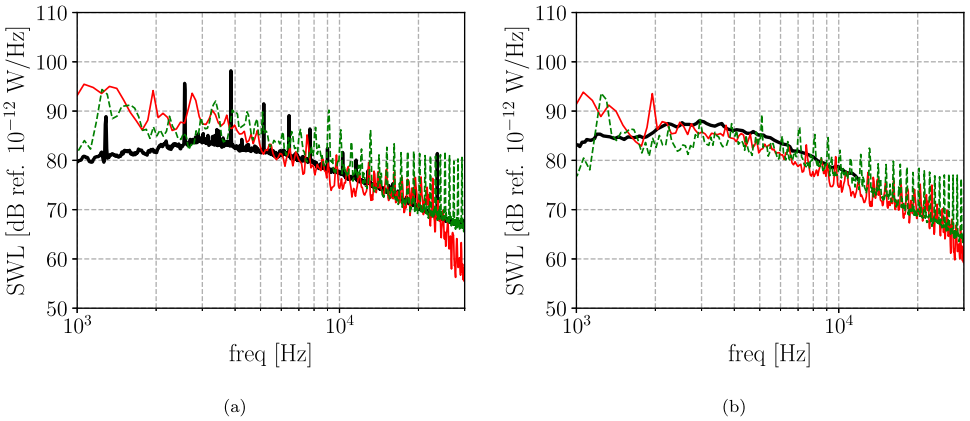

Fig. 39. Upstream SWL (left) and downstream SWL (right) spectra obtained from Goldstein's analogy (LES1: 10 windows, LES2: 5 windows). Experiment (——), LES1 (——), LES2 (- - -).

important contributor to the overall stator noise in LES2, despite the absence of any flow separations on the stator suction side. This suggests that the disappearance of the flow separation in the LES2 is not responsible on its own of the low frequency noise reduction with respect to LES1 predictions. The transition of the boundary layer occurring on the stator suction side is most likely responsible for a major part of the noise radiated by the stator, in both simulations. As with the LES1 predictions, the front and aft parts are strongly correlated, which suggests a potential downstream shift of the LE source. These observations all show that the noise mechanisms related to the boundary layer, its turbulent transition and its scattering by the trailing edge, also play an important role in the broadband noise production. Similar observations were made by De Laborderie et al. [60,63] on a low-pressure compressor that exhibited unexpected dominant broadband noise sources in addition to the RSI mechanism. Polacsek et al. [24] carried out a similar study by splitting the ACAT OGV at 50% chord and observed a significant contribution of the aft part of the OGV, which is around 5 dB higher than the front part contribution, whereas in the present case the gap is about 10 dB. This increased difference is caused not only by the more intense TE secondary sources in the present study with respect to Polacsek et al.'s results [24], but also by the fact that the front part of the OGV in their computation encompasses secondary noise sources, the intensity of which is of the same order of magnitude as the RSI sources (as mentioned in Section 5.1). Furthermore, Polacsek et al.'s study [24] was performed using Goldstein's analogy, whereas FW-H analogy was used in the present case, which may have an impact on the relative contribution of each part of the OGV since the duct cut-off effect may affect them differently. These observations tend to support the actual presence of significant secondary noise sources at the aft part of the OGV, while they could have been considered as numerical artifacts in the first place. The disparity in the secondary source magnitude prediction may stem from the fact that the involved flow phenomena are actually particularly challenging to capture. In the present case, an overestimation of their intensity might be responsible for the remaining overestimation observed in the LES2 noise predictions. Finally, as the shielding effect of the rotor is not accounted for with this approach, the higher downstream noise usually observed when studying the RSI mechanism is not recovered with the present noise assessments. Taking this into account would significantly improve the prediction as a noise reduction of 3 dB in the upstream direction and a similar increase in the downstream direction would be expected at approach conditions [68]. Fig. 42 shows that the LES2 predictions are in very good agreement with the noise measurements when considering such an indicative rotor shielding correction.

5.3.2. Rotor noise

Noise predictions using the pressure fluctuations recorded on the rotor skin have been performed for both LES. The results are plotted in Fig. 43. The LES1 and LES2 spectra are consistent with the observations made in Section 4.3.2. The LES1 leading-edge vortex tends to create larger and stretched structures, which results in higher noise levels at low frequencies and lower ones at high frequencies. On the contrary, the LES2 leading-edge vortex creates smaller structures, which leads to spectra that look like the LES1 ones but tilted anticlockwise since lower noise levels are found at low frequencies, while higher ones are observed at high frequencies. In terms of magnitude, the rotor noise of both LES display comparable and even higher levels than the noise radiated by the front part of their respective stator. In the case of LES2, the rotor produces noise levels above 8 kHz that are similar to those produced by the entire OGV. Hence, the rotor significantly takes part in the broadband noise production, because of the intense LE vortex, of the turbulent structures it generates, but also because of the scattering of the latter structures and of the induced turbulent boundary layer by the trailing edge. These sources were also identified by Deuse et al. [51] and Wu et al. [52] in their study of the CD airfoil self-noise, at a much lower chord based Reynolds number ($\approx 10^5$), and were shown to be amplified at Mach numbers close to that of the present configuration. Al Am et al. [54] also studied these sources on a fan-OGV configuration of limited spanwise extent, and showed that the LE flow separation was linked to two self noise mechanisms: a tonal noise mechanism directly resulting from the recirculation bubble itself, and a broadband noise mechanism generated by the scattering of the turbulent boundary layer. Consequently, even-though the dominant sources seem to be located on the stator, the rotor noise sources are far from being negligible and must be accounted for in the noise assessment to provide accurate predictions.

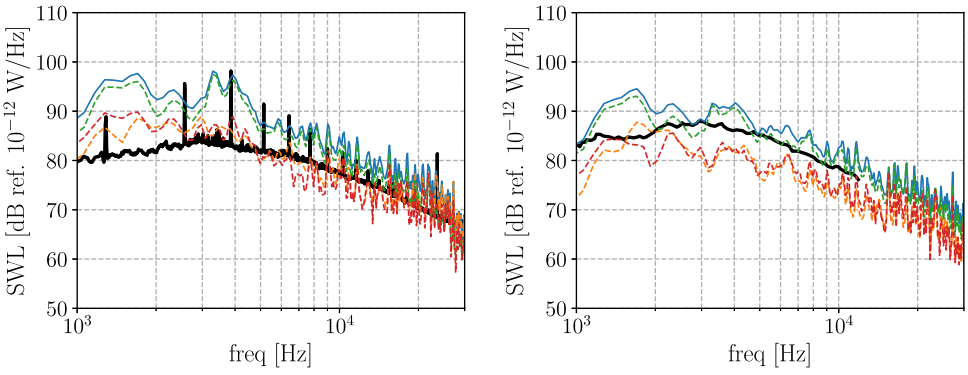

Fig. 40. LES1 upstream SWL (left) and downstream SWL (right) spectra obtained from Ffowcs Williams and Hawkings' analogy, for each sub-part of the vane (10 windows). Experiment (——), Full vane (——), Front part (- - -), Aft part (- - -), Cross-correlation (- - -).

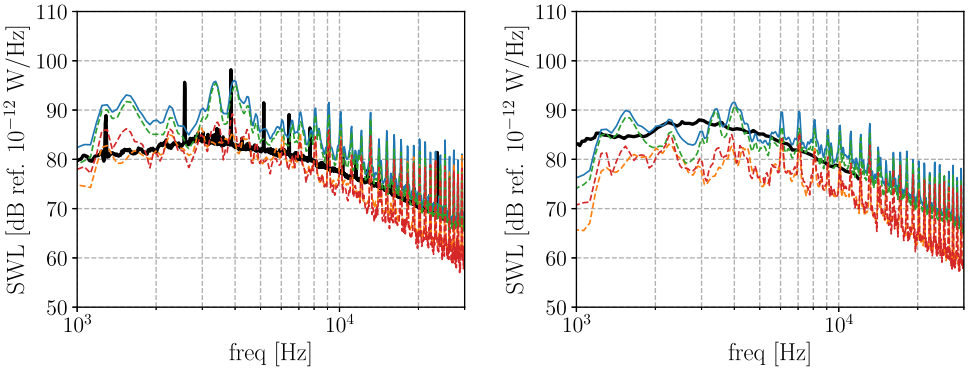

Fig. 41. LES2 upstream SWL (left) and downstream SWL (right) spectra obtained from Ffowcs Williams and Hawkings' analogy, for each sub-part of the vane (5 windows). Experiment (——), Full vane (——), Front part (- - -), Aft part (- - -), Cross-correlation (- - -).

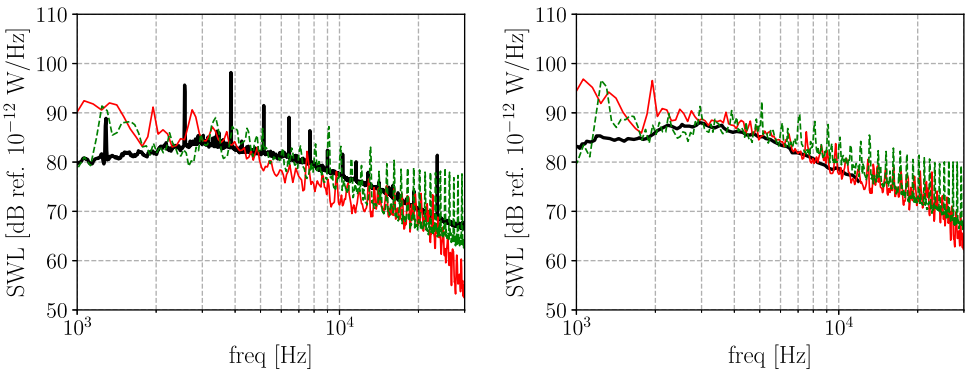

Fig. 42. Upstream SWL (left) and downstream SWL (right) spectra obtained from Goldstein's analogy (LES1: 10 windows, LES2: 5 windows). Experiment (——), LES1 (——), LES2 (- - -). Rotor shielding effect correction (−3 dB upstream, +3 dB downstream) applied to LES1 and LES2 results.

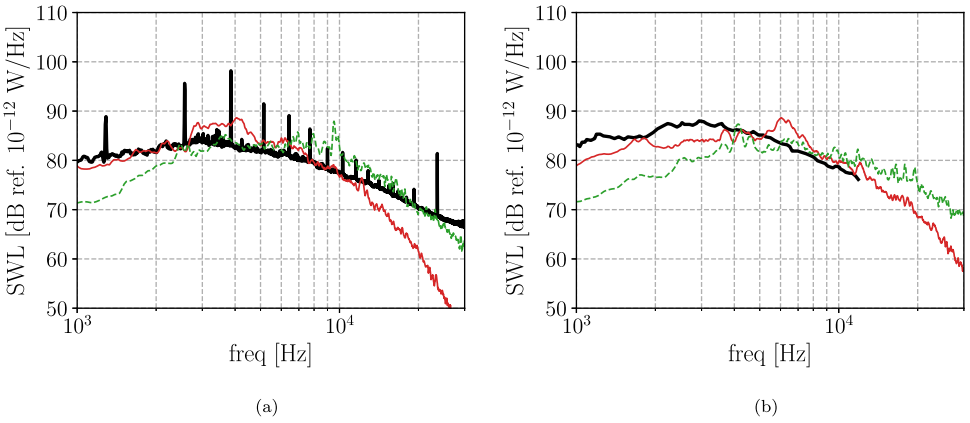

Fig. 43. Upstream SWL (left) and downstream SWL (right) spectra obtained from Ffowcs Williams and Hawkings analogy (3 windows for both simulations). Experiment (——), LES1 (——), LES2 (- - -).

6. Conclusion

A noise assessment of the ACAT1 configuration at approach condition has been carried out using a hybrid noise computation approach. Two wall-modeled LES with different levels of mesh refinement have been performed, LES2 having a finer mesh than LES1. Both simulations have shown a good agreement with the experimental performance parameters, with a slight deviation of the LES2 mass-flow rate resulting from a significant modification of the flow topology on the stator suction side. The stator flow detachment observed in LES1 totally disappears in LES2 because of the mesh refinement, despite the fact that both meshes actually meet the mesh requirements for wall modeled LES. In both simulations, a boundary layer transition is observed at mid-chord. The flow topology near the rotor blade remains almost unchanged from LES1 to LES2, only the magnitude of the phenomena slightly decreased. Both simulations exhibit a strong radial vortical structure at the rotor leading-edge, which is typical of fans operating at approach conditions. Despite slight inconsistencies in the hot-wire measurements, especially regarding the radial component of the velocity, a great improvement of the mean flow velocity profiles has been observed in LES2 with respect to LES1. Though still slightly overestimated, the LES2 RMS profiles and velocity spectra are much closer to the measurements than those of LES1, showing the mandatory aspect of using a finer mesh in this context. The analysis of the pressure fluctuations on the rotor and stator surfaces has revealed three main broadband noise mechanisms:

- The rotor leading edge radial vortical structure, the subsequent boundary layer transition, and its scattering by the trailing edge.
- The RSI sources, located at the stator leading-edge.
- The stator boundary layer transition and its scattering by the trailing-edge.

Noise predictions have been performed using the pressure fluctuations recorded on both stator and rotor surfaces as dipole sources in the framework of both the free-field FW-H analogy, and the in-duct Goldstein analogy. Great improvements of the noise predictions have been observed with the finer LES2 mesh. The predictions have also highlighted the need to take into account the duct cut-off effect, as more accurate noise predictions have been obtained with Goldstein's analogy. The stator noise source breakdown has revealed that the contribution of the turbulent boundary layer scattering by the trailing edge could exceed that of the RSI mechanism, even though the latter has remained significant. Accurately predicting the intensity of these OGV secondary noise sources is still challenging because of the complex involved flow phenomena. Yet, both present LES and a parallel ZDES have confirmed their existence and physical relevance. Moreover, a significant broadband noise contribution of the rotor sources has been highlighted, especially at medium and high frequencies for which it compares with the stator contribution. These results question the common assumption considering the RSI mechanism as the only dominant broadband noise source within a fan stage at approach condition, making it possible to envision new ways to reduce broadband noise emissions. One of the main perspectives for the present study would be to consider a full 360° simulation, with direct acoustic propagation up to the limit of the computational domain to avoid resorting to acoustic analogies and alleviate the assumptions made on the rotor shielding effect.

CRediT authorship contribution statement

Danny Lewis: Conceptualization, Methodology, Validation, Investigation, Writing – original draft, Formal analysis, Visualization, Writing – review & editing. **Stéphane Moreau:** Conceptualization, Methodology, Resources, Writing – review & editing, Supervision, Funding acquisition. **Marc C. Jacob:** Conceptualization, Methodology, Resources, Writing – review & editing, Supervision, Funding acquisition. **Marlène Sanjosé:** Conceptualization, Methodology, Software, Validation, Investigation, Formal analysis, Visualization, Writing – review & editing.

Declaration of competing interest

The authors declare that they have no known competing financial interests or personal relationships that could have appeared to influence the work reported in this paper.

Data availability

The authors do not have permission to share data

Acknowledgments

This study was carried out in the framework of the project TurboNoiseBB, that was funded by the European Union's Horizon 2020 research and innovation program under the grant agreement number 690714. The research was conducted in the framework of the LABEX CeLyA (ANR-10-LABX-0060), a research network funded via the program "Investissements d'Avenir" (ANR-16-IDEX-0005) operated by the French National Research Agency (ANR). The computational resources were provided by the GENCI network (CINES-OCCIGEN, project number A0062A06074), by CERFACS, and by PMCS2I-FLMSN. The authors wish to thank the members of the TurboNoiseBB consortium for providing experimental data and for fruitful discussions throughout the project and in particular R. Barrier (ONERA) who kindly provided the rescaled outlet guide vane. M. Sanjosé's contribution to this work essentially consisted in developing and providing the annular duct formulation of the FW-H analogy as well as guidelines for its practical application. In this context, the numerous discussions with P. Khodolov (UdS) on the subtleties of the Goldstein formulation were also of great interest. The authors want to thank N. Odier, M. Fiore and F. Duchaine from CERFACS for their help to obtain computational resources on GENCI's cluster as well as their advice on the use of AVBP and the exploitation of its results. Most of the LES postprocessing was performed using Antares (release 1.15.0, https://www.cerfacs.fr/antares).

References

[1] N. Peake, A.B. Parry, Modern challenges facing turbomachinery aeroacoustics, Annu. Rev. Fluid Mech. 44 (2012) 227–248, URL https://doi.org/10.1146/annurev-fluid-120710-101231.
[2] S. Moreau, Turbomachinery noise predictions: present and future, Acoustics 1 (1) (2019) 92–116.
[3] D. Lewis, J. de Laborderie, M. Sanjosé, S. Moreau, M.C. Jacob, V. Masson, Parametric study on state-of-the-art analytical models for fan broadband interaction noise predictions, J. Sound Vib. 514 (116423) (2021) URL https://doi.org/10.1016/j.jsv.2021.116423.
[4] S. Moreau, M. Roger, Advanced noise modeling for future propulsion systems, Int. J. Aeroacoustics 17 (6–8) (2018) 576–599.
[5] M. Wang, J.B. Freund, S.K. Lele, Computational prediction of flow-generated sound, Annu. Rev. Fluid Mech. 38 (2006) 483–512, URL https://doi.org/10.1146/annurev.fluid.38.050304.092036.
[6] J.E. Ffowcs Williams, D.L. Hawkings, Sound generation by turbulence and surfaces in arbitrary motion, Philos. Trans. R. Soc. Lond. Ser. A Math. Phys. Eng. Sci. 264 (1151) (1969) 321–342, URL https://doi.org/10.1098/rsta.1969.0031.
[7] M.E. Goldstein, Aeroacoustics, McGraw-Hill International Book Co., New York, 1976, p. 305, (1976).
[8] I. Gonzalez-Martino, D. Casalino, Fan tonal and broadband noise simulations at transonic operating conditions using lattice-Boltzmann methods, in: 2018 AIAA/CEAS Aeroacoustics Conference, no. 2018–3919, Atlanta, Georgia, 2018, URL https://doi.org/10.2514/6.2018-3919.
[9] D. Casalino, A. Hazir, A. Mann, Turbofan broadband noise prediction using the lattice Boltzmann method, AIAA J. 56 (2) (2018) 609–628, URL https://doi.org/10.2514/1.J055674.
[10] D. Casalino, A.F. Ribeiro, E. Fares, S.E. Noelting, A. Mann, F. Perot, Y. Li, P.-T. Lew, C. Sun, P. Gopalakrishnan, et al., Towards lattice-Boltzmann prediction of turbofan engine noise, in: 20th AIAA/CEAS Aeroacoustics Conference, no. 2014–3101, Atlanta, Georgia, 2014, URL https://doi.org/10.2514/6.2014-3101.
[11] T. Leonard, M. Sanjose, S. Moreau, F. Duchaine, Large eddy simulation of a scale-model turbofan for fan noise source diagnostic, in: 22nd AIAA/CEAS Aeroacoustics Conference, no. 2016–3000, Lyon, France, 2016, pp. 1–23, URL https://doi.org/10.2514/6.2016-3000.
[12] C. Pérez Arroyo, T. Leonard, M. Sanjosé, S. Moreau, F. Duchaine, Large eddy simulation of a scale-model turbofan for fan noise source diagnostic, J. Sound Vib. 445 (2019) 64–76, URL https://doi.org/10.1016/j.jsv.2019.01.005.
[13] P. Kholodov, C. Pérez Arroyo, M. Sanjosé, S. Moreau, Fan broadband noise computation at transonic regime, in: 25th AIAA/CEAS Aeroacoustics Conference, no. 2019–2714, Delft, The Netherlands, 2019, URL https://doi.org/10.2514/6.2019-2714.
[14] C. Polacsek, M. Daroukh, B. François, R. Barrier, Turbofan broadband noise predictions based on a ZDES calculation of a fan-OGV stage, in: 9th Forum Acusticum, 2020.
[15] P. Kholodov, S. Moreau, Identification of noise sources in a realistic turbofan rotor using large eddy simulation, Acoustics 2 (3) (2020) 691–706, http://dx.doi.org/10.3390/acoustics2030037, URL https://www.mdpi.com/2624-599X/2/3/37.
[16] D. Lewis, S. Moreau, M.C. Jacob, Broadband noise predictions on the ACAT1 fan stage using large eddy simulations and analytical models, in: AIAA AVIATION 2020 FORUM, no. 2020–2519, VIRTUAL EVENT, 2020, URL https://arc.aiaa.org/doi/10.2514/6.2020-2519.
[17] D. Lewis, S. Moreau, M.C. Jacob, ACAT1 fan stage broadband noise prediction using large-eddy simulation and analytical models, AIAA J. 60 (1) (2022) URL https://arc.aiaa.org/doi/pdf/10.2514/1.J060163.
[18] R. Meyer, S. Hakansson, W. Hage, L. Enghardt, Instantaneous flow field measurements in the interstage section between a fan and the outlet guiding vanes at different axial positions, in: Proceedings of 13th European Conference on Turbomachinery Fluid Dynamics and Thermodynamics, Lausanne, Switzerland, April, 2019, pp. 8–12, URL https://doi.org/10.29008/ETC2019-330.
[19] M. Behn, U. Tapken, Investigation of sound generation and transmission effects through the ACAT1 fan stage using compressed sensing-based mode analysis, in: 25th AIAA/CEAS Aeroacoustics Conference, no. 2019–2502, Delft, The Netherlands, 2019, URL https://doi.org/10.2514/6.2019-2502.
[20] U. Tapken, M. Behn, M. Spitalny, B. Pardowitz, Radial mode breakdown of the ACAT1 fan broadband noise generation in the bypass duct using a sparse sensor array, in: 25th AIAA/CEAS Aeroacoustics Conference, no. 2019–2525, Delft, The Netherlands, 2019, URL https://doi.org/10.2514/6.2019-2525.
[21] H. Brouwer, P. Sijtsma, Phased array beamforming to identify broadband noise sources in the interstage section of a turbofan engine, in: 25th AIAA/CEAS Aeroacoustics Conference, no. 2019–2669, Delft, The Netherlands, 2019, URL https://doi.org/10.2514/6.2019-2669.
[22] D. Lewis, S. Moreau, M.C. Jacob, On the use of RANS-informed analytical models to perform broadband rotor-stator interaction noise predictions, in: 25th AIAA/CEAS Aeroacoustics Conference, no. 2019–2667, Delft, The Netherlands, 2019, URL https://doi.org/10.2514/6.2019-2667.

[23] B. François, C. Polacsek, R. Barrier, Zonal Detached Eddy Simulation of the Fan-Outlet Guide Vanes Stage of a Turbofan Engine: Part I—Methodology, Numerical Setup, and Aerodynamic Analysis, J. Turbomach. 144 (11) (2022) 111004, URL https://doi.org/10.1115/1.4054528.

[24] C. Polacsek, M. Daroukh, B. François, R. Barrier, Zonal Detached Eddy Simulation of the Fan-Outlet Guide Vanes Stage of a Turbofan Engine: Part II—Broadband Noise Predictions, J. Turbomach. 144 (11) (2022) 111005, URL https://doi.org/10.1115/1.4054764.

[25] S. Deck, Recent improvements in the zonal detached eddy simulation (ZDES) formulation, Theor. Comput. Fluid Dyn. 26 (2012) 523–550, URL https://doi.org/10.1007/s00162-011-0240-z.

[26] C. Lowis, P. Joseph, A. Kempton, Estimation of the far-field directivity of broadband aeroengine fan noise using an in-duct axial microphone array, J. Sound Vib. 329 (19) (2010) 3940–3957, URL https://doi.org/10.1016/j.jsv.2010.03.021.

[27] U. Tapken, B. Pardowitz, M. Behn, Radial mode analysis of fan broadband noise, in: 23rd AIAA/CEAS Aeroacoustics Conference, 2017, p. 3715, URL https://doi.org/10.2514/6.2017-3715.

[28] R. Bauers, U. Tapken, Separation of hydrodynamic perturbations in acoustic liner insertion loss measurements at a fan rig, in: 18th AIAA/CEAS Aeroacoustics Conference (33rd AIAA Aeroacoustics Conference), 2012, p. 2277, URL https://doi.org/10.2514/6.2012-2277.

[29] B. François, R. Barrier, C. Polacsek, Zonal detached eddy simulation of the fan-OGV stage of a modern turbofan engine, in: ASME Turbo Expo 2020: Turbine Technical Conference and Exposition, American Society of Mechanical Engineers Digital Collection, 2020, URL https://hal.archives-ouvertes.fr/hal-03048643.

[30] M.M. Rai, N.K. Madavan, Multi-Airfoil Navier–Stokes Simulations of Turbine Rotor–Stator Interaction, J. Turbomach. 112 (3) (1990) 377–384, URL https://doi.org/10.1115/1.2927670.

[31] D. Lewis, From Analytical to Fully Numerical Predictions of the Broadband Noise Radiated by a Full Fan-OGV Stage, 2020.

[32] T. Schönfeld, M. Rudgyard, Steady and unsteady flow simulations using the hybrid flow solver AVBP, AIAA J. 37 (11) (1999) 1378–1385, URL https://doi.org/10.2514/2.636.

[33] G. Wang, F. Duchaine, D. Papadogiannis, I. Duran, S. Moreau, L.Y. Gicquel, An overset grid method for large eddy simulation of turbomachinery stages, J. Comput. Phys. 274 (July 2015) (2014) 333–355, http://dx.doi.org/10.1016/j.jcp.2014.06.006.

[34] P.D. Lax, B. Wendroff, Difference schemes for hyperbolic equations with high order of accuracy, Comm. Pure Appl. Math. 17 (3) (1964) 381–398, URL https://doi.org/10.1002/cpa.3160170311.

[35] F. Nicoud, F. Ducros, Subgrid-scale stress modelling based on the square of the velocity gradient tensor, Flow Turbul. Combust. 62 (3) (1999) 183–200, arXiv:arXiv:1503.01439v1.

[36] T.J. Poinsot, S. Lelef, Boundary conditions for direct simulations of compressible viscous flows, J. Comput. Phys. 101 (1) (1992) 104–129, URL https://doi.org/10.1016/0021-9991(92)90046-2.

[37] N. Odier, M. Sanjosé, L. Gicquel, T. Poinsot, S. Moreau, F. Duchaine, A characteristic inlet boundary condition for compressible, turbulent, multispecies turbomachinery flows, Comput. & Fluids 178 (2019) 41–55, URL https://doi.org/10.1016/j.compfluid.2018.09.014.

[38] E. Nicoud, O. Colin, C. Angelberger, F. Nicollet, C. Krüger, A no-slip implementation of a wall law boundary condition in a cell-vertex code for LES of internal aerodynamics on unstructured meshes, in: Conference LES4ICE, IFP Energies Nouvelles, Rueil-Malmaison, 2016.

[39] P. Schmitt, T. Poinsot, B. Schuermans, K. Geigle, Large-eddy simulation and experimental study of heat transfer, nitric oxide emissions and combustion instability in a swirled turbulent high-pressure burner, J. Fluid Mech. 570 (2007) 17–46, URL https://doi.org/10.1017/S0022112006003156.

[40] G. Wang, S. Moreau, F. Duchaine, J. De Laborderie, L. Gicquel, LES investigation of aerodynamics performance in an axial compressor stage, in: 22nd Annual Conference of the CFD Society of Canada, Toronto, Canada, June, 2014, pp. 1–4.

[41] G. Wang, S. Moreau, F. Duchaine, N. Gourdain, L. Gicquel, Large eddy simulations of the MT1 high-pressure turbine using turboavbp, in: Proceeding of 21st Annual Conference of the CFD Society of Canada, Sherbrooke, Quebec, Canada, 2013, pp. 70–106.

[42] N. Odier, F. Duchaine, L. Gicquel, G. Staffelbach, A. Thacker, N. García Rosa, G. Dufour, J.-D. Muller, Evaluation of integral turbulence scale through the fan stage of a turbofan using hot wire anemometry and large eddy simulation, in: ASME Turbo Expo 2018: Turbomachinery Technical Conference and Exposition, American Society of Mechanical Engineers Digital Collection, 2018, URL https://doi.org/10.1115/GT2018-75741.

[43] C. Pérez Arroyo, J. Dombard, F. Duchaine, L. Gicquel, B. Martin, N. Odier, G. Staffelbach, Towards the large-eddy simulation of a full engine: Integration of a 360 azimuthal degrees fan, compressor and combustion chamber. Part I: Methodology and initialisation, J. Glob. Power Propuls. Soc. (May) (2021) URL https://doi.org/10.33737/jgpps/133115.

[44] C. Pérez Arroyo, J. Dombard, F. Duchaine, L. Gicquel, B. Martin, N. Odier, G. Staffelbach, Towards the large-eddy simulation of a full engine: Integration of a 360 azimuthal degrees fan, compressor and combustion chamber. Part II: Comparison against stand-alone simulations, J. Glob. Power Propuls. Soc. (May) (2021) URL https://doi.org/10.33737/jgpps/133116.

[45] U. Piomelli, Large eddy simulations in 2030 and beyond, Phil. Trans. R. Soc. A 372 (2022) (2014) URL https://doi.org/10.1098/rsta.2013.0320.

[46] C. Wagner, T. Hüttl, P. Sagaut, Large-eddy simulation for acoustics, 2007, p. 20, URL https://doi.org/10.1017/CBO9780511546143.

[47] C. Mockett, T. Knacke, F. Thiele, Detection of initial transient and estimation of statistical error in time-resolved turbulent flow data, in: 8th International Symposium on Engineering Turbulence Modelling and Measurements (ETMM8), Marseille, France, June, 2010, pp. 9–11.

[48] C. Kissner, S. Guérin, P. Seeler, M. Billson, C. Paruchuri, P. Carrasco Laraña, H. de Laborderie, B. François, K. Lefarth, D. Lewis, G. Montero Villar, T. Nodé-Langlois, ACAT1 benchmark of RANS-informed analytical methods for fan broadband noise prediction: Part I - Influence of the RANS simulation, in: Acoustics, Multidisciplinary Digital Publishing Institute, 2020, URL https://doi.org/10.3390/acoustics2030029.

[49] C. Pérez Arroyo, T. Leonard, M. Sanjosé, S. Moreau, F. Duchaine, Large eddy simulation of a rotor stage for fan noise source diagnostic, in: Proceedings of the Global Power and Propulsion Forum, Montreal, QC, Canada, 2018, pp. 7–9, URL https://pdfs.semanticscholar.org/d8cb/d363906249e6c93318cdaefe6edf04859516.pdf.

[50] P. Kholodov, R. Koch, M. Sanjosé, S. Moreau, Wall-Resolved Large Eddy Simulation of a Realistic Turbofan Rotor for Noise Prediction, arXiv:https://arc.aiaa.org/doi/pdf/10.2514/6.2021-2256. URL https://arc.aiaa.org/doi/abs/10.2514/6.2021-2256.

[51] M. Deuse, R.D. Sandberg, Different noise generation mechanisms of a controlled diffusion aerofoil and their dependence on mach number, J. Sound Vib. 476 (2020) 115317, URL https://doi.org/10.1016/j.jsv.2020.115317.

[52] H. Wu, S. Moreau, R. Sandberg, On the noise generated by a controlled-diffusion aerofoil at $Re_c = 1.5 \times 10^5$, J. Sound Vib. 506 (2020) 116152: 1–20, http://dx.doi.org/10.1017/jfm.2019.129.

[53] P.G. Tucker, Z.-N. Wang, Eddy resolving strategies in turbomachinery and peripheral components, J. Turbomach. 143 (1) (2021).

[54] J. Al-Am, V. Clair, A. Giauque, J. Boudet, F. Gea-Aguilera, On the effects of a separation bubble on fan noise, J. Sound Vib. 537 (2022) 117180, URL https://doi.org/10.1016/j.jsv.2022.117180.

[55] J. Maunus, S. Grace, D. Sondak, Effect of CFD wake prediction in a hybrid simulation of fan broadband interaction noise, in: 17th AIAA/CEAS Aeroacoustics Conference (32nd AIAA Aeroacoustics Conference), no. 2011–2875, Portland, Oregon, 2011, URL https://doi.org/10.2514/6.2011-2875.

[56] R. Meyer, S. Hakansson, W. Hage, L. Enghardt, Instantaneous flow field measurements in the interstage section between a fan and the outlet guiding vanes at different axial positions, in: Proc. the 13th European Conference on Turbomachinery Fluid Dynamics and Thermodynamics, no. ETC2019-330, 2019.

[57] L. Caldas, C. Kissner, M. Behn, U. Tapken, R. Meyer, Comparison of techniques for the estimation of flow parameters of fan inflow turbulence from noisy hot-wire data, Fluids 6 (11) (2021) 372, URL https://doi.org/10.3390/fluids6110372.

[58] F. Perot, S. Moreau, M.-S. Kim, M. Henner, D. Neal, Direct aeroacoustics predictions of a low speed axial fan, in: 16th AIAA/CEAS Aeroacoustics Conference, no. 2010–3887, Stockholm, Sweden, 2010, URL https://doi.org/10.2514/6.2010-3887.

[59] J. Al Am, V. Clair, A. Giauque, J. Boudet, F. Gea-Aguilera, Direct noise predictions of fan broadband noise using LES and analytical models, in: 28th AIAA/CEAS Aeroacoustics 2022 Conference, 2022, p. 2882, URL https://doi.org/10.2514/6.2022-2882.
[60] J. de Laborderie, S. Moreau, A. Berry, Compressor stage broadband noise prediction using a large-eddy simulation and comparisons with a cascade response model, in: 19th AIAA/CEAS Aeroacoustics Conference, no. 2013–2042, 2013, URL https://doi.org/10.2514/6.2013-2042.
[61] A. Pereira, M.C. Jacob, Modal analysis of in-duct fan broadband noise via an iterative Bayesian inverse approach, J. Sound Vib. 520 (2022) 116633, http://dx.doi.org/10.1016/j.jsv.2021.116633.
[62] H. Posson, S. Moreau, M. Roger, Broadband noise prediction of fan outlet guide vane using a cascade response function, J. Sound Vib. 330 (25) (2011) 6153–6183, URL https://doi.org/10.1016/j.jsv.2011.07.040.
[63] J. De Laborderie, Approches analytiques et numériques pour la prédiction du bruit tonal et large bande de soufflantes de turboréacteurs (Ph.D. thesis), 2013, doi:http://hdl.handle.net/11143/6121. URL http://savoirs.usherbrooke.ca/handle/11143/6121.
[64] A. Fosso Pouangué, M. Sanjosé, S. Moreau, G. Daviller, H. Deniau, Subsonic jet noise simulations using both structured and unstructured grids, AIAA J. 53 (1) (2015) 55–69.
[65] D. Casalino, An advanced time approach for acoustic analogy predictions, J. Sound Vib. 261 (4) (2003) 583–612, URL https://doi.org/10.1016/S0022-460X(02)00986-0.
[66] A. Najafi-Yazdi, G.A. Brès, L. Mongeau, An acoustic analogy formulation for moving sources in uniformly moving media, Proc. R. Soc. A 467 (2125) (2011) 144–165, URL https://doi.org/10.1098/rspa.2010.0172.
[67] J.E. Ffowcs Williams, D.L. Hawkings, Sound generation by turbulence and surfaces in arbitrary motion, Philos. Trans. R. Soc. Lond. Ser. A Math. Phys. Eng. Sci. 264 (1151) (1969) 321–342, URL https://doi.org/10.1098/rsta.1969.0031.
[68] R. Blázquez-Navarro, R. Corral, Prediction of fan acoustic blockage on fan/outlet guide vane broadband interaction noise using frequency domain linearised Navier–Stokes solvers, J. Sound Vib. 500 (2021) 116033, URL https://doi.org/10.1016/j.jsv.2021.116033.